Article

Cell

EGFR Dynamics Change during Activation in Native Membranes as Revealed by NMR

Graphical Abstract

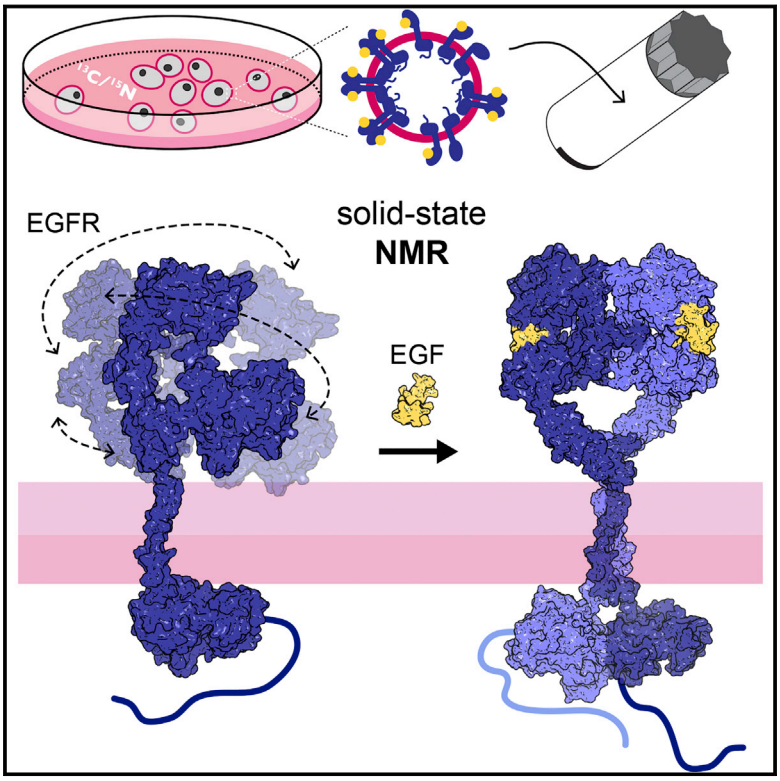

Highlights

- NMR can be applied to study activation of full-length EGFR in native membranes
- Solid-state NMR provides insight into structure and mobility of full-length EGFR
- Data identify conformational selection as a key factor for receptor activation

Authors

Mohammed Kaplan, Siddarth Narasimhan, Cecilia de Heus, ..., Simone Lemeer, Paul M.P. van Bergen en Henegouwen, Marc Baldus

Correspondence

p.vanbergen@uu.nl (P.M.P.v.B.e.H.), m.baldus@uu.nl (M.B.)

In Brief

An NMR approach shows how receptors move in native membranes at high resolution, revealing that, while the intracellular domain of EGFR is rigid, the extracellular domain is highly dynamic until bound by ligand.

Kaplan et al., 2016, Cell *167*, 1241–1251
November 17, 2016
http://dx.doi.org/10.1016/j.cell.2016.10.038

CellPress

Article

Cell

EGFR Dynamics Change during Activation in Native Membranes as Revealed by NMR

Mohammed Kaplan,[1,5] Siddarth Narasimhan,[1] Cecilia de Heus,[2,6] Deni Mance,[1] Sander van Doorn,[3] Klaartje Houben,[1] Dušan Popov-Čeleketić,[2] Reinier Damman,[1] Eugene A. Katrukha,[2] Purvi Jain,[2] Willie J.C. Geerts,[4] Albert J.R. Heck,[3] Gert E. Folkers,[1] Lukas C. Kapitein,[2] Simone Lemeer,[3] Paul M.P. van Bergen en Henegouwen,[2,*] and Marc Baldus[1,7,*]

[1]NMR Spectroscopy, Bijvoet Center for Biomolecular Research

[2]Cell Biology, Department of Biology, Faculty of Science

[3]Biomolecular Mass Spectrometry and Proteomics, Bijvoet Center for Biomolecular Research and Utrecht Institute for Pharmaceutical Sciences

[4]Biomolecular Imaging, Bijvoet Center for Biomolecular Research

Utrecht University, 3584 CH Utrecht, the Netherlands

[5]Present address: Physical Biology Center for Ultrafast Science and Technology, Arthur Amos Noyes Laboratory of Chemical Physics, California Institute of Technology, Pasadena, CA 91125, USA

[6]Present address: University Medical Center Utrecht, Cell Biology, Heidelberglaan 100, 3584CX Utrecht, the Netherlands

[7]Lead Contact

*Correspondence: p.vanbergen@uu.nl (P.M.P.v.B.e.H.), m.baldus@uu.nl (M.B.)

http://dx.doi.org/10.1016/j.cell.2016.10.038

SUMMARY

The epidermal growth factor receptor (EGFR) represents one of the most common target proteins in anti-cancer therapy. To directly examine the structural and dynamical properties of EGFR activation by the epidermal growth factor (EGF) in native membranes, we have developed a solid-state nuclear magnetic resonance (ssNMR)-based approach supported by dynamic nuclear polarization (DNP). In contrast to previous crystallographic results, our experiments show that the ligand-free state of the extracellular domain (ECD) is highly dynamic, while the intracellular kinase domain (KD) is rigid. Ligand binding restricts the overall and local motion of EGFR domains, including the ECD and the C-terminal region. We propose that the reduction in conformational entropy of the ECD by ligand binding favors the cooperative binding required for receptor dimerization, causing allosteric activation of the intracellular tyrosine kinase.

INTRODUCTION

The epidermal growth factor receptor (EGFR, Her1, or ErbB1) is one of the four members of the Her (ErbB) family of receptor tyrosine kinases that serves as cell-surface receptor for peptide ligands and plays a crucial role in regulating cell proliferation, migration, and differentiation (Arteaga and Engelman, 2014; Ferguson et al., 2003; Yarden, 2001). ErbB proteins are linked to the development of different tumors (e.g., colorectal carcinoma, head and neck cancer, and gliomas) and represent a successful target for anti-cancer therapies using antibodies or small molecules inhibitors (Tebbutt et al., 2013).

EGFR consists of an extracellular domain (ECD) formed by domains I to IV, a single-pass transmembrane (TM) domain, a juxtamembrane (JM) region, a tyrosine kinase domain (KD), and a C-terminal-region (CT), in which multiple potential tyrosine kinase substrate residues are located. Detailed structural information has been obtained for various EGFR segments, such as the ECD (Ferguson et al., 2003; Garrett et al., 2002; Ogiso et al., 2002) and the KD (Jura et al., 2009; Stamos et al., 2002), or for constructs containing the TM and JM domains in membrane mimetics (Endres et al., 2013; Lu et al., 2010; Stamos et al., 2002). Crystal structures have furthermore suggested that the non-liganded ECD can adapt a closed conformation that is stabilized by an intramolecular tether between domain II and IV (Ferguson et al., 2003; Ogiso et al., 2002). On the other hand, the liganded ECD was found in an open, extended conformation leading to the intracellular active KD. Significant progress has been made in deciphering which interaction sites are involved in the stabilization of the EGFR dimer. They include the dimerization loops in domain II (Dawson et al., 2005), the GxxxG or GG4 motifs in the TM (Lu et al., 2010), the antiparallel coiled coils in the JM (Doerner et al., 2015), and the KD (Jura et al., 2009). These multiple interactions contribute to the cooperative formation and stabilization of the dimer of the wild-type (Dawson et al., 2005) and, at least partially, of tumor-related constitutively active EGFR mutants (Valley et al., 2015).

In spite of these studies, a unified structural view that describes the ligand-induced functional coupling between the ECD and the intracellular domain of the full-length receptor in a native membrane environment has remained elusive (Bessman et al., 2014; Kovacs et al., 2015). FRET, as well as molecular dynamics (MD) studies using EGFR in synthetic lipid bilayers, suggest that the unliganded EGFR ECD is located close to the membrane in the closed, tethered conformation (Arkhipov et al., 2013; Kaszuba et al., 2015; Ziomkiewicz et al., 2013). However, recent MD data from the ECD without membrane show a highly flexible fold (Arkhipov et al., 2013), which would explain the dynamic existence of predimers on cell surfaces (Low-Nam et al., 2011). MD studies furthermore suggest that the dimerized EGFR ectodomain is lying flat on the membrane, thereby possibly explaining

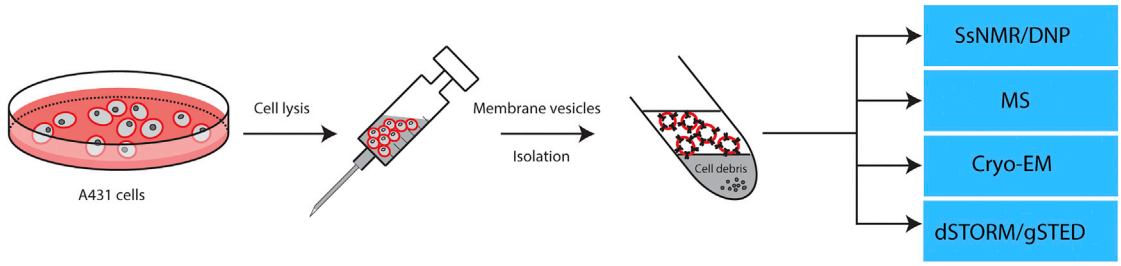

Figure 1. Preparation of EGFR-Rich Membrane Vesicles from A431 Cells

Schematic presentation for the preparation of A431 membrane vesicles. For MS/EM/dSTORM/gSTED studies, cells were grown on DMEM medium, while for ssNMR studies, A431 cells were cultured in [^{13}C, ^{15}N]-labeled DMEM medium (~20 plates were required for one sample). Cells were scraped from the plates and vesiculated by passing them through a syringe 10 times. After removal of the unbroken cells and cell nuclei by spinning at low speed, the membrane vesicles were spun down at high speed and loaded into an ssNMR rotor. Note that all methods can also be used to study whole cells.

the negative cooperativity of ligand binding (Arkhipov et al., 2014). On the other hand, recent FRET studies speak in favor of an increased distance between domain I and the membrane after ligand binding in line with an upright position of the dimerized ECDs (Valley et al., 2015; Ziomkiewicz et al., 2013).

These studies, together with previous work highlighting the influence of native membrane lipids such as cholesterol (den Hartigh et al., 1992) or gangliosides (Coskun et al., 2011; Miljan and Bremer, 2002), as well as receptor glycosylation (Liu et al., 2011) for receptor activation and internalization, underline the notion that a comprehensive understanding of receptor activation requires the study of the full-length EGFR in its native environment. To address this aspect, we describe in the following the development and application of a solid-state NMR (ssNMR)-based approach to directly examine structural and dynamical properties of full-length EGFR in native membrane vesicles before and after activation. Unlike solution-state NMR, where small membrane proteins such as the transmembrane region of EGFR can be studied in membrane mimetics (Endres et al., 2013), ssNMR can give detailed structural insight into the role of the bilayered membrane for protein structure in synthetic (Matsushita et al., 2013) or native bacterial membranes (Kaplan et al., 2015) largely irrespective of their size and mobility. In addition, ssNMR can probe changes in local or overall protein dynamics at ambient temperature by the reduction in signal intensity in dipolar-based experiments due to the presence of motion (Etzkorn et al., 2010; Hong et al., 2012; Schneider et al., 2010) and by tracking ssNMR line width variations due to backbone fluctuations at low temperatures (Koers et al., 2014). Importantly, the latter studies are fully compatible with sensitivity enhancement methods such as dynamic nuclear polarization (DNP) that results in NMR signal enhancements by one to two orders of magnitude (Ni et al., 2013). The combination of this high-sensitivity technique with tailored amino-acid labeling allows for the study of local protein structure even in complex molecular environments (Kaplan et al., 2015).

To investigate EGFR in its native membrane environment by ssNMR, we utilized A431 cells to extract EGFR-enriched membrane vesicles amenable for NMR studies. For reference, we characterized these membrane vesicle preparations by electron microscopy, super-resolution light microscopy, and mass spectrometry (MS). Using previous structural information obtained for EGFR domains (Ferguson et al., 2003; Lu et al., 2010; Ogiso et al., 2002; Stamos et al., 2002) and assuming the C-terminal domain to be unstructured, we monitored EGFR structure and dynamics at global and residue-specific levels. Taken together, our NMR data reveal dynamics of specific EGFR regions in the unliganded state, which are strongly reduced by ligand binding, suggesting that a reduction in conformational entropy contributes to the free energy of EGFR dimerization.

RESULTS

Isolation and Characterization of EGFR-Rich A431 Membrane Vesicles

To investigate EGFR in its native membrane environment, we used A431 cells known to exhibit a high (1–2 × 10^6 receptors per cell) expression level of EGFR (Haigler et al., 1978) to produce EGFR-containing membrane vesicles amenable for our multi-technique approach (Figure 1). Confocal microscopy of A431 cells and EGFR negative cells confirmed high-level expression of EGFR (Figure 2A). In addition, super-resolution light microscopy (dSTORM) experiments using anti-EGFR nanobodies and cryo-electron microscopy revealed the isolation of vesicles with a size of 50–250 nm, with EGFR localized to the membrane (Figures 2B and 2C). To determine the orientation of EGFR in these vesicles, we treated the vesicles with Proteinase K for 15 min at 4°C and analyzed the samples by western blotting using an antibody specific for the intracellular domain. Comparison of the EGFR protein band intensity using densitometry with the remaining intracellular domain band of 65 kDa suggests that approximately 85% ± 6.4 (mean ± SEM, n = 3) of EGFR is in the right outside-out orientation (Figure 2D). This was confirmed by three-color gated stimulated emission depletion (gSTED) microscopy, where the vesicles were stained with the lipophylic membrane stain DiI, EGF-A488, and an anti-EGFR nanobody conjugated to A647 (NB-A647). Almost all vesicles showed EGF binding (Figure 2E). Fluorescence intensity analysis of colocalized vesicles shows a high degree of correlation between the EGF-A488 and NB-A647 (Pearson correlation coefficient: $r = 0.577$, $N = 84$, $p < 0.001$) (Figure 2F). In addition, we observed ligand-induced phosphorylation (Figure 2G), confirming high-level expression of functionally active EGFR in the isolated membrane vesicles. To probe the level of EGFR expression, we

conducted MS experiments on A431 cells and the isolated membrane vesicles (Figure 3). Using an accepted semiquantitative approach based on summed ions intensities over all detected peptides we found actin to be the most abundant protein in whole A431 cells, followed by other abundant soluble molecules including heat shock and histone proteins. While the EGFR expression level was lower than these proteins, EGFR still represented the most abundant membrane protein in our cells in line with previous findings (Haigler et al., 1978). When moving to isolated membrane vesicles, we found EGFR highly enriched by a factor 5.5 (Figure 3), making EGFR, together with actin, the most abundant protein in our membrane vesicles. As membrane proteins, such as EGFR, are typically less detectable by MS than soluble proteins (Santoni et al., 2000), such as actin, we argue that the MS-based estimation of EGFR levels is at the lower limit. In summary, our results shown in Figures 2 and 3 confirmed the presence of high levels of functional EGFR in our isolated membrane vesicles. Such preparations are also advantageous with respect to the amount of protein in our ssNMR experiments, and we consequently prepared vesicles amenable for ssNMR studies by growing A431 cells on a medium containing [^{13}C, ^{15}N]-labeled algae mixture (Figure 1).

Solid-State NMR Experiments on [^{13}C, ^{15}N]-Labeled A431 Membrane Vesicles at Ambient Temperatures Suggest a Dynamic Extracellular Domain and Rigid Kinase Domain

Using [^{13}C, ^{15}N]-labeled A431 vesicles, we examined the effect of the addition of EGF (Figures 4 and S1) and of variations in temperature (253 and 285 K, Figures S1 and S2) on the resulting 1D and 2D ssNMR spectra. While signal intensities in frozen samples in the absence or presence of EGF were very comparable (Figure S1C), ssNMR intensities differed at ambient temperature, with a clear increase in signal intensity after addition of EGF (Figures S1D and 4), indicative of a ligand-induced structural stabilization of EGFR. Moreover, the overall 2D correlation pattern seen at lower temperatures (Figure S2) correlated with chemical-shift predictions on the basis of previous EGFR domain structures (Ferguson et al., 2003; Garrett et al., 2003; Lu et al., 2010; Ogiso et al., 2002; Stamos et al., 2002) and assuming the C-terminal (CT) domain to be unstructured. These observations confirmed the dominance of folded EGFR in our spectra (Figure S2). SsNMR signals from our vesicular samples remained constant during extended measurement periods, consistent with intact protein preparations (Figure S3). Next to the folded protein signals, we also observed mobile random-coil signals from unstructured protein regions (such as the EGFR CT) and other small molecules, including lipids and sugars (Figure S4).

Spectral overlap precluded an analysis of the entire 1,186-amino-acid receptor by conventional ssNMR. However, 2D (^{13}C,^{13}C) double-quantum/single quantum experiment (DQSQ) (Figure 4A) spectra at ambient temperatures provided sufficient spectral resolution to investigate changes in ssNMR signal intensities and peak positions in different 2D segments, such as the Ser and Thr spectral region (Figures 4B and 4C), as well as regions containing Ala (Figure 4D) and Pro (Figure 4E) residues. Using standard secondary chemical-shift values (Wang and Jardetzky, 2002), we distinguished spectral regions characteristic for α-helical (red boxes), random-coil (rc, black boxes), and β strand (blue boxes) for backbone Ca (dashed line) and Cb (solid line) resonances, and we estimated, based on the EGFR amino-acid sequence and the available structures, the relative contribution (equivalent to the total expected NMR signal intensity) of the major receptor segments, i.e., ECD, KD, and CT. Such an analysis was also performed for actin (Figure S5).

The observation that EGF induces spectral changes (Figure 4) already provided a strong indication that the ssNMR data at high temperatures were dominated by signals of the EGFR receptor, where actin monomers may be too mobile to be detected. This notion was further confirmed by analyzing ssNMR correlations for specific residue types and secondary structure elements presented in the following (see Figure S5 for a statistical analysis of protein secondary structure and amino-acid distributions for EGFR and actin). Examining the Ser-region before EGF binding, we observed Ser signals mostly in α-helical conformations and additional intensity matching Ser in random-coil conformations (Figure 4B). A dominant α-helical signal before addition of EGF can only be explained by the EGFR KD domain (Figure 4B), and the significant increase in β strand and random-coil signals would be compatible with an increasing contribution of ECD (for both β strand and random coil conformations) and CT (random coil conformations) EGFR domains after EGF binding. Interestingly, such a notion correlates with signal changes in the Thr (Figure 4C) and Ala region (Figure 4D), where α-helical correlations are dominant and β strand/random-coil contributions appear after EGF binding. A similar effect would explain the strong signal increase in the Pro signals, which are most abundant in EGFR ECD and CT, after EGF binding. Taken together, these observations (which we confirmed by repeating experiments on different sample batches) suggest that the ssNMR data (Figure 4) are dominated by a rigid KD domain of EGFR in the resting state and the appearance of rigid ECD domain and possibly the CT domain of EGFR after EGF binding. Note, however, that such a global analysis of our ssNMR spectra does not allow us to unambiguously identify structural changes in the CT domain and to draw general conclusions about the much-smaller TM and JM domains or individual residues.

DNP-Supported Solid-State NMR Experiments on Specifically [^{13}C, ^{15}N]-Labeled A431 Vesicles Detect a Reduction in Local Protein Dynamics after Ligand Binding

In order to obtain site-specific information of the different domains of EGFR, we produced specifically [^{13}C, ^{15}N]-labeled A431 membrane vesicles with ^{13}C-Met, ^{13}C-Phe, ^{15}N-Thr, and ^{15}N-Leu (referred to henceforth as MFTL-labeled EGFR). As shown before (Kaplan et al., 2015), this strategy introduced atomic probes that lead to residue-specific sequential correlations in inter-residue ssNMR, the so-called NCOCX, experiments. This approach generates, in total, 12 sequential residue pairs in the two most-abundant proteins in our samples, namely, EGFR and actin. Nine of these sequential correlations are distributed in EGFR extracellular domains D1–D3, the intracellular tyrosine KD, and the CT (Figure 5A), while the remaining three correlations result from actin (PDB: 1D4X, Figure S6A). Due to a limited signal-to-noise ratio at higher temperatures, we resorted to DNP

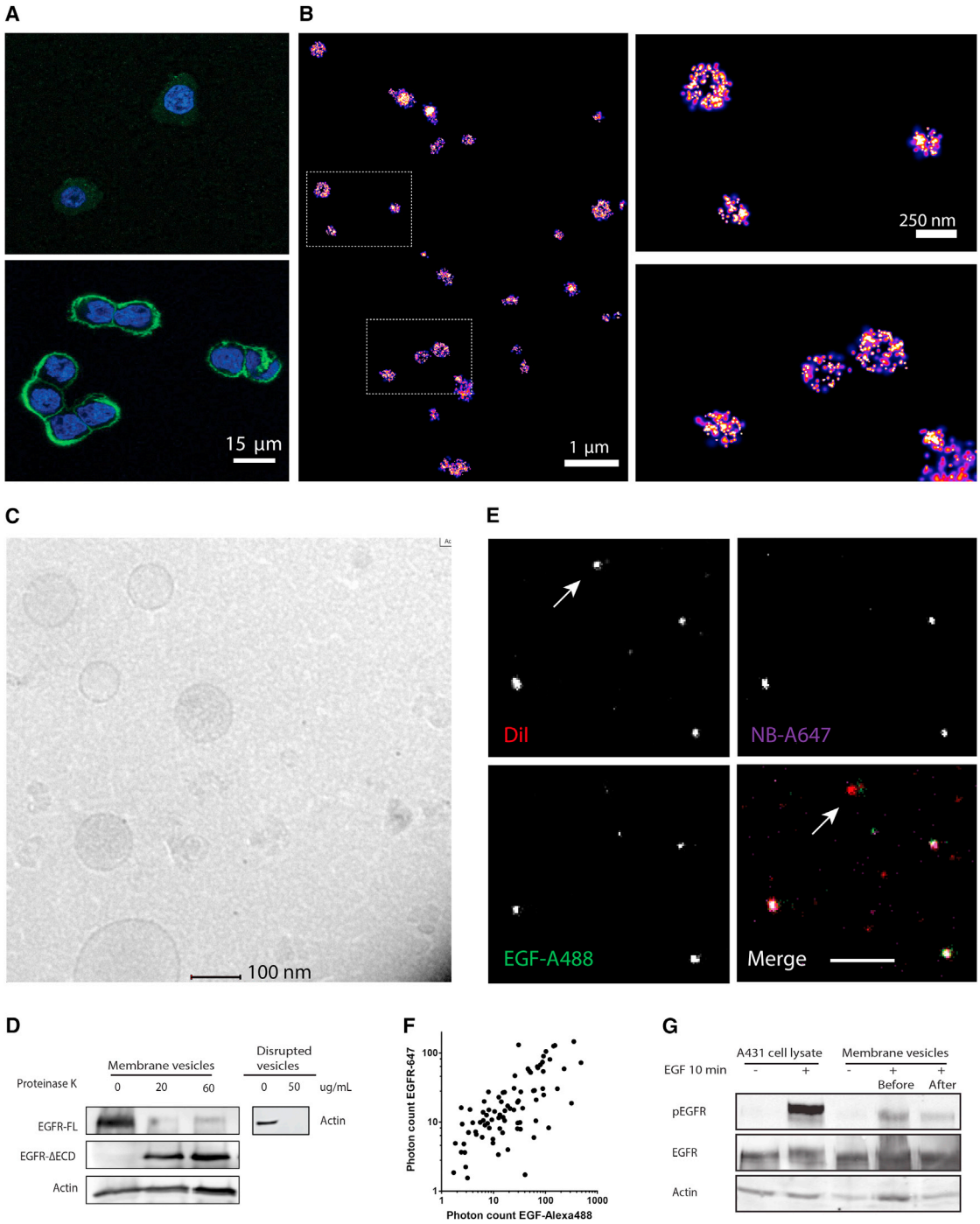

Figure 2. Structural and Functional Characterization of A431 Cells and Membrane Vesicles

(A) Confocal microscopy of A431 cells (bottom) and NIH 3T3 clone 2.2 cells (EGFR negative) (top) incubated with Alexa488-tagged EGF (in green). Blue represents DAPI staining of nuclei.

(B) dSTORM reconstruction of A431 vesicles stained with anti-EGFR, Alexa647-conjugated nanobody (left), and two magnified 3-μm^2 areas (right). Scale bars indicate 1 μm and 250 nm, respectively.

(C) Cryo-EM of A431 membrane vesicles. The sample was observed without chemical fixation or contrast.

(D) Western blot analysis of proteinase-K-treated vesicles to determine EGFR topology in the membrane vesicles. Freeze/thaw-disrupted membrane vesicles were used to confirm proteinase K activity. EGFR_FL: full-length EGFR; EGFR-ΔECD: EGFR lacking the ECD.

(E) Three-color gSTED imaging of A431 vesicles labeled with a membrane dye (DiI), EGF-A488, and an anti-EGFR nanobody conjugated to Alexa647. Arrows indicate DiI stained vesicles not labeled with EGF or anti-EGFR NB. Scale bar indicates 1 μm.

(legend continued on next page)

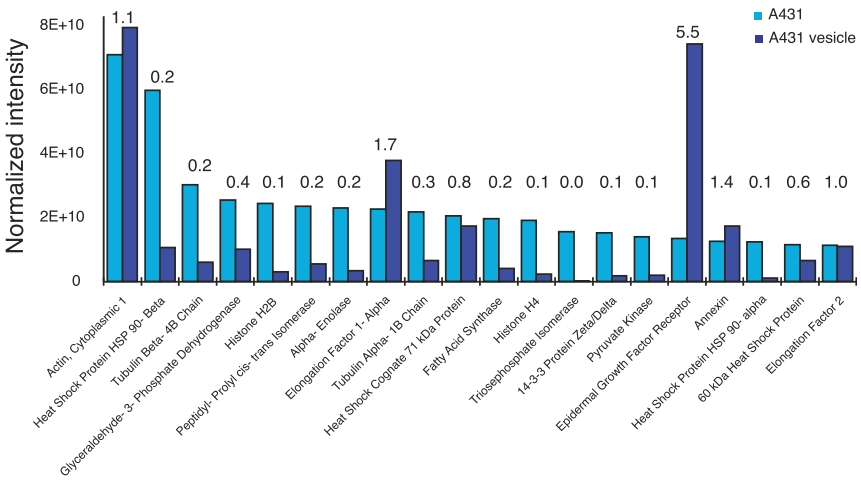

Figure 3. Relative Abundance of EGFR in A431 Cells and Membrane Vesicles Assessed by Mass Spectrometry

Normalized intensities of the 20 most-abundant proteins in intact A431 cells (light blue) and corresponding intensities in membrane vesicles (dark blue). Intensities were calculated by summing the intensities over all peptides detected in the tryptic digests of the cells and vesicles for the annotated proteins. Intensities were normalized to the sum of peptide intensities detected in both vesicles and the whole-cell lysates. From the normalized intensities, enrichment factors (labels) were calculated, clearly revealing that of the 20 most-abundant proteins in cells, only EGFR is highly enriched in the membrane vesicles.

experiments, which significantly increase NMR signal intensity via electron polarization (Ni et al., 2013). The increased sensitivity (with a DNP enhancement factor $\varepsilon \sim 20$ at 800 MHz and ~ 80 at 400 MHz) allowed us to perform 2D and 3D NCOCX experiments at 400 (Figures 5B, 5D, and 5E) and 800 (Figure S6B) MHz DNP conditions, as well as a 2D ^{15}N-edited ^{13}C-^{13}C experiment (Baker et al., 2015) at 400 MHz DNP conditions (Figure 5C). Again, we made use of standard spectral regions expected for α-helix (red), β strand (blue), and random-coil (black) ssNMR frequencies for both ^{13}C and ^{15}N dimensions. These spectral regions are indicated for expected Phe and Met correlations by solid and dashed lines in Figures 5B–5E, respectively.

In general, the addition of EGF can lead to chemical-shift or line-width changes in ssNMR data of EGFR due to local alterations in protein structure and dynamics or due to the presence of a nearby ligand. Interestingly, the addition of EGF significantly increased spectral resolution both in NC (Figures 5B, 5D, and 5E and S6), as well as in ^{15}N-edited CC (Figure 5C) experiments, indicative of a reduction in local backbone and side-chain fluctuations that reduce line broadening at low temperatures (Koers et al., 2014) and a dominant contribution of EGFR correlations to the spectrum. In line with the latter conclusions, we found the most-dominant signals in Phe α-helical and random-coil regions (Wang and Jardetzky, 2002) in full analogy to the expected three correlations for EGFR in domain I and in domain III, as well as in the CT, respectively (Figure 5A). In addition, we found at an ^{15}N chemical shift of 124 ppm (Figure 5B, NCOCX experiment), which is characteristic for Leu residues in β strand or random-coil conformations, and a clear β strand Phe correlation in our ^{15}N-edited ^{13}C-^{13}C experiment (Figure 5C) that can only stem from EGFR, namely, the sequential pair ^{380}FL^{381} in domain III (Figure 5A, denoted Phe$_\beta$(1,0) in Figure 5B). In the crystal structure (Ogiso et al., 2002), the ^{380}FL^{381} pair is located close to the EGF binding site (see Figures 6A and 6B), which would readily explain the observed chemical-shift changes for the tentatively identified correlation in Figure 5C. We also observe a clear shift and spectral changes after EGF binding in the random-coil Phe Cβ region, which strongly suggests that these signals stem from ^{357}FT^{358} (D3), as well as from the two sequential correlations in the CT (as indicated in Figure 5C).

In full accordance with a dominant contribution of EGFR to our spectra, we did not observe methionine correlations in β strand conformations (indicated Met$_\beta$(0,0) in Figure 5C). Instead, we detected Met correlations (which can be discriminated on the basis of their characteristic Cb shifts) in α-helix and random-coil conformations, in line with EGFR and actin predictions. In summary, our spectra at DNP temperatures (100°K) suggested the dominant role of EGFR signals also in our LT-DNP spectra. For both EGF-free and EGF-bound conformations, our observed correlations globally matched with expectations from previous X-ray structures of the corresponding EGFR subdomains, and we could tentatively assign chemical-shift changes to a residue pair located close to the EGF binding site previously seen in protein crystals. In addition, our ssNMR data suggested a significant reduction in local backbone and side-chain fluctuations that would give rise to structural disorder at low temperatures before EGF binding.

DISCUSSION

Increasing evidence suggests that a comprehensive view of EGFR activation requires the study of structure and dynamics of the full-length receptor in its native cell membrane setting (Bessman et al., 2014; Kovacs et al., 2015). NMR has, for a long time, contributed to obtaining such information for molecules that tumble rapidly under in vitro (Arkhipov et al., 2013; Kern and Zuiderweg, 2003; Kerns et al., 2015; Nygaard et al., 2013) and, more recently, under in-cell conditions (Banci et al., 2013; Serber et al., 2001; Smith et al., 2015). On the other hand, ssNMR provides increasing possibilities to conduct such

(F) Scatterplot of integrated fluorescence intensities of individual A431 membrane vesicles in EGF-A488 and anti-EGFR NB-647 channels.

(G) Phosphorylation assay of A431 plasma membrane vesicles to detect phosphorylated EGFR (pEGFR) with anti-P1068 antibody. A431 cells were incubated at 37°C with (+) or without (−) EGF for 10 min. For membrane vesicles samples, either A431 cells were incubated at 37°C for 10 min with EGF (+), followed by vesicle preparation, or vesicles were first prepared from A431 cells, after which they were incubated at 37°C without (−) or with (+) EGF.

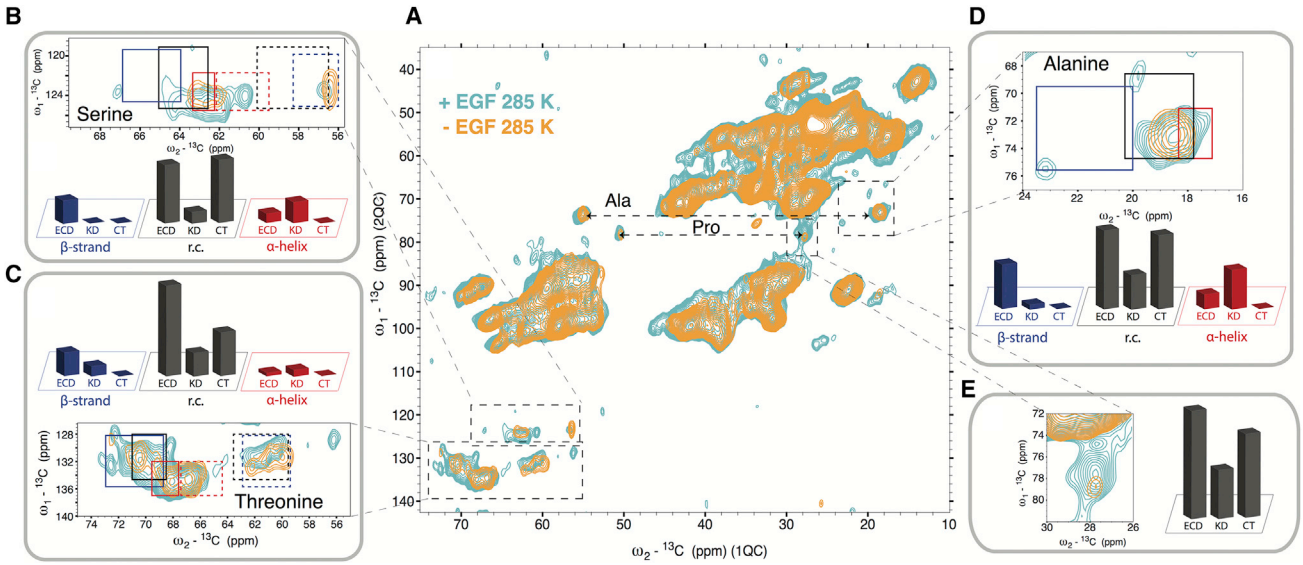

Figure 4. EGF-Induced Alterations in Dynamics of Fully [^{13}C, ^{15}N]-Labeled EGFR as Seen by 2D ssNMR at Ambient Temperatures

(A) DQSQ of fully [^{13}C, ^{15}N]-labeled A431 vesicles without EGF (orange) and with EGF (cyan) at 285°K.

(B–E) Zoom-in of spectral regions comprising serine, threonine, alanine, and proline resonances. Solid lines and dashed boxes represent the Cb and Ca chemical-shift regions in α-helix (red), β sheet (blue), and random-coil (black) conformations, respectively. Scale bars (normalized for each amino acid type) reflect the number of residues expected to occur in the three considered backbone structural folds (B–D) or the total number of residues (E) in the ECD, KD, and CT domain. The analysis was performed using the known structures of different EGFR domains.

See also Figures S1, S2, S3, S4, and S5.

studies on large, possibly membrane-embedded, protein complexes in their natural cell environment (Chow et al., 2014; Frederick et al., 2015; Kaplan et al., 2015; Renault et al., 2012). Here, we have shown how to extend such studies to examine large eukaryotic protein receptors in their native membrane setting by isolating fully and specifically [^{13}C, ^{15}N]-labeled membrane vesicles that express the functional receptor of interest to high levels. Combining 2D ssNMR data at ambient temperatures with DNP studies of specifically labeled membrane vesicles allowed us to examine the overall structure and dynamics of the full-length EGFR before and after ligand binding in situ.

Taken together, our ssNMR analysis suggests that the observed spectroscopic changes due to EGF binding are largely due to alterations in receptor dynamics. Before activation, our data are in accordance with a highly dynamic ECD and CT and a rigid KD, in line with earlier studies suggesting autoinhibitory interactions of the KD and the N-terminal portions of the intracellular JM region with the intracellular membrane surface (Endres et al., 2013; Sengupta et al., 2009) (Figures 6A and 6B). The fluctuations (local and global) of the ECD in the absence of EGF preclude strong interactions of the ECD with the membrane, which is in disagreement with recent MD studies on the EGFR ECD domain (Arkhipov et al., 2013). Rather, our experimental results are in line with experimental results (Coskun et al., 2011; den Hartigh et al., 1992; Liu et al., 2011; Miljan and Bremer, 2002) and recent computational studies (Kaszuba et al., 2015) suggesting a key role for the natural composition of the cell membrane and receptor glycosylation for receptor dynamics. Indeed, we observed in our ssNMR experiments additional mobility in other endogenous cellular components, including lipids and sugars, suggesting the presence of receptor dynamics at different timescales in our samples (Figure S4).

Our results suggest a model for EGFR activation in which the ECD is present on the cell surface of resting cells as an ensemble of different conformers. Both the closed, tethered conformation can be expected, as well as the open conformation in which the autoinhibitory tether between domain II and IV is released (Figure 6A). Based upon a previously suggested ΔG of 1 to 2 kcal/mole of the domain II/IV interaction, 80%–97% of the ECD was expected in the closed conformation (Ferguson et al., 2003). In this framework, global and local dynamics probed in our ssNMR studies would be most compatible with the presence of global domain motions of large portions of the ECD combined with local backbone fluctuations (detected by DNP-ssNMR for the EGF binding region, as well as the dimerization interface, Figure 6B) that can lead to the open conformation, enabling the ectodomain to form inactive (pre)dimers previously detected for very short time periods (Low-Nam et al., 2011). The highly dynamic nature of the unliganded EGFR also explains the ligand-independent dimerization and activation of EGFR at higher expression levels of EGFR in the plasma membrane of different cancer cells. The ECD dynamics result in the presence of the ECD in the extended conformation, which is prone to form dimers. Since the percentage of extended conformations will not change, the number of EGFRs in the extended conformation is higher, resulting in a higher probability for predimer formation. Similarly, it explains the observation that the ECD in active EGFR mutants can lead to enhanced ligand-independent dimerization (Valley et al., 2015). Deletion of parts of the ECD as has occurred in viral

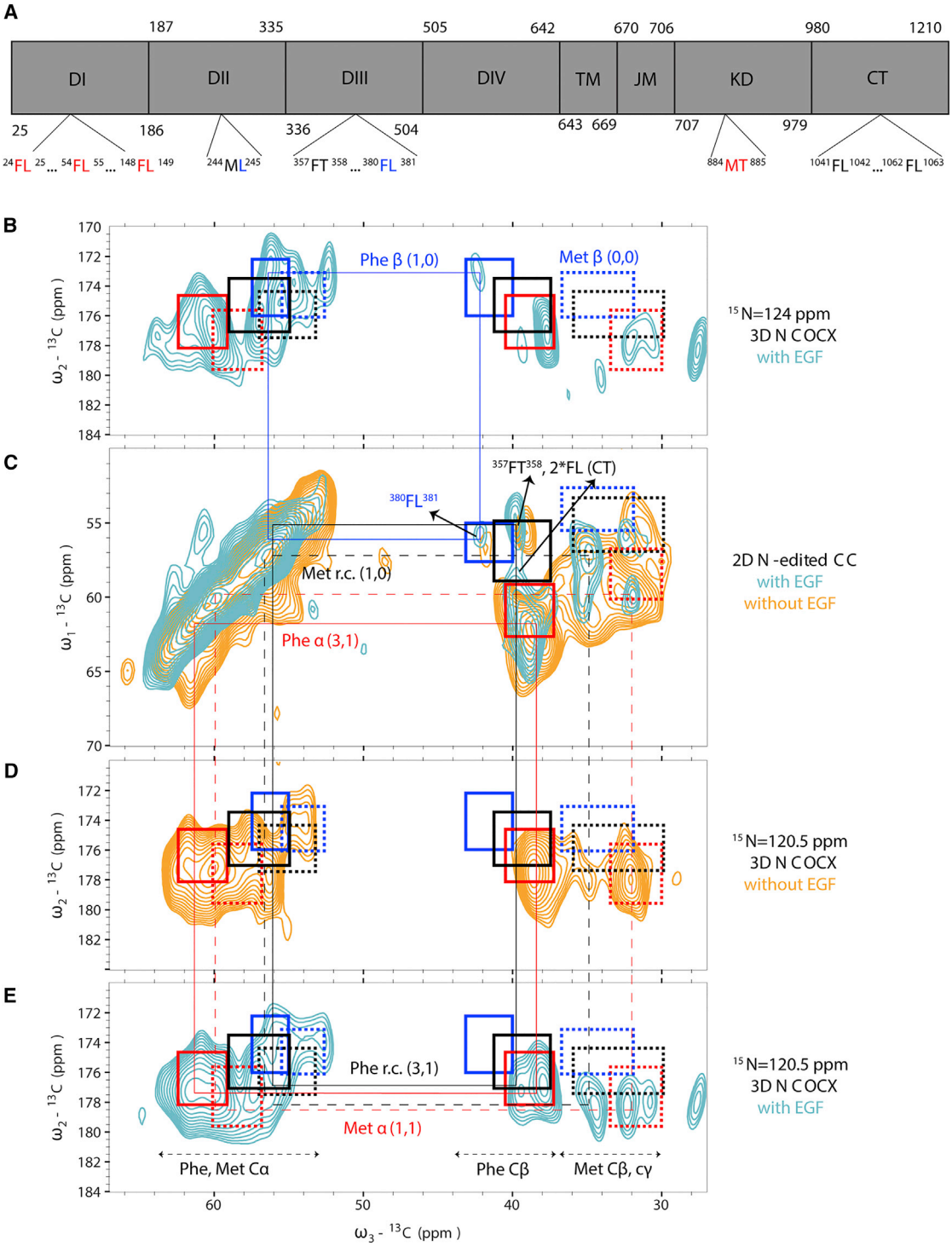

Figure 5. DNP-ssNMR Experiments on MFTL-Labeled A431 Vesicles Reveal Ligand-Induced Protein Stabilization on the Level of Individual Residues

(A) Schematic view of EGFR domains, highlighting the sequential correlations expected in a ^{13}C-[F, M] and ^{15}N-[L, T] labeled sample. Color-coding stands for specific backbone conformations as described in the main text.

(B, D, and E) 2D planes of 3D NCOCX experiments before (D, orange) and after (B and E, cyan) addition of EGF for the indicated ^{15}N chemical shifts.

(C) 2D N-edited ^{13}C-^{13}C experiment of MFTL A431 membrane obtained with (cyan) and without (orange) EGF. In (B–E), red, blue, and black boxes represent the chemical-shift ranges expected for Phe (solid lines) and Met (dotted lines) Ca and Cb correlations in α-helical, random-coil, and β strand conformations.

(legend continued on next page)

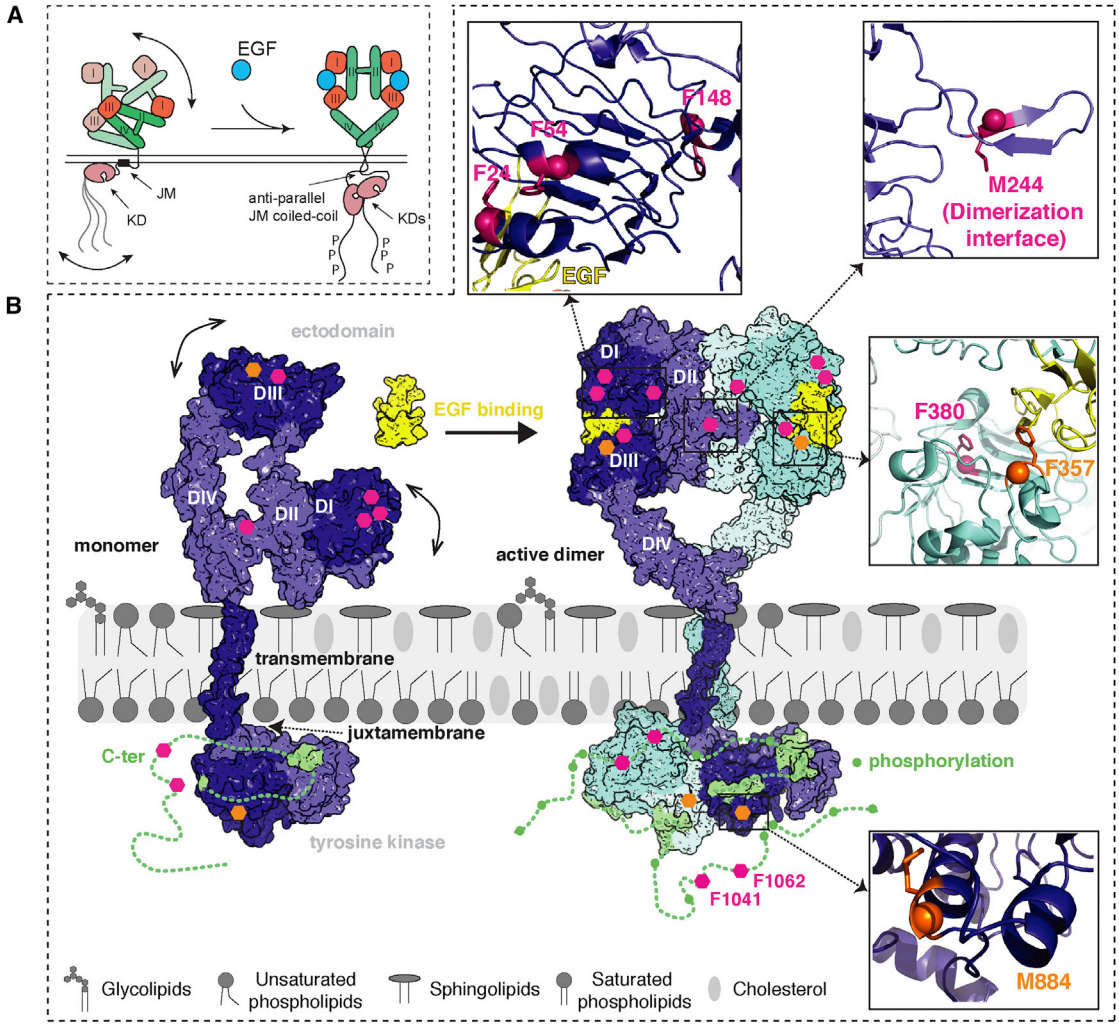

Figure 6. A Model of EGFR Dynamics and Structural Changes in the Free and EGF-Bound Forms

(A) Generic model of EGFR activation via conformational selection in the ECD.

(B) At high temperatures (285°K), the unbound receptor exhibits dynamics in both the ECD and CT. Upon binding to the ligand EGF (shown in yellow), the receptor dimerizes and exhibits less dynamics, both on a global and local scale. Residues probed by ssNMR in the MFTL sample are highlighted in orange (MT and FT residue pairs) and magenta (ML and FL pairs), and zoom-ins show local protein structure. ^{13}C-labeled residues (M and F) contain side-chains in stick representation, and the ^{15}N-labeled residues (T and L) are represented as spheres on the backbone nitrogen.

and oncogenic variants as v-ERB and EGFviii release the closed conformation, resulting in a larger number of less-stable ligand-independent dimers. As a consequence, basal kinase activity levels are higher but less than EGF-induced kinase activity.

We hypothesize that EGF binding can occur to all conformers, including the open conformation. In this model, EGF does not induce a conformational change of the receptor but rather stabilizes the open conformation, which is preceding receptor dimerization. The reduced dynamics of the liganded EGFR result in a rigid conformation with reduced conformational entropy, which contributes to the binding of the multiple low-affinity interaction motifs that are present not only in the ECD (Dawson et al., 2005) but in the entire EGFR. This cooperative binding of two rigid EGFR monomers involves the tether in domain II, GxxxG, or GG4 motifs in the TM, the anti-parallel α helices in the JM, as well as the KD domain (Doerner et al., 2015; Ferguson et al., 2003; Jura et al., 2009; Lu et al., 2010). In this way, the reduction in global, as well as local, dynamics contributes to the

Connecting lines track experimentally observed Phe (solid lines, annotated by Phe [X,Y]) and Met (dashed lines, annotated by Met [X,Y]) correlations in α-helical, β strand, and random-coil conformations, respectively. X,Y stand for the number of predicted sequential correlations for X = EGFR and Y = Actin on the basis Figure 5A (EGFR) and Figure S6A (Actin). In (C), tentative assignments for the ^{380}FL^{381} pair, as well as for the spectral correlations consistent with signals stemming from ^{357}FT^{358} (DIII) and from the two sequential correlations in the CT, are indicated. All experiments were conducted at 400 MHz DNP conditions. See also Figures S5 and S6.

cooperative binding of EGFR monomers by an entropy-enthalpy compensation mechanism.

Analogous to emerging signal-transduction mechanisms across cell membranes (Nygaard et al., 2013), the concept of an allosteric regulation in which a reduction in receptor dynamics may be sufficient to shift the conformational equilibrium from inactive monomers and inactive predimers to EGF-activated EGFR populations may also help to understand ligand-induced dimerization of other receptor tyrosine kinases. Our presented ssNMR approach may furthermore aid the refinement of structure and dynamics of such membrane-embedded EGFR populations, including the domain IV region containing glycosylated sites critical for ligand binding (Whitson et al., 2005) and the C-terminal domain of EGFR. Such studies may provide critical insight into the role of the plasma membrane and receptor dynamics in related eukaryotic growth factor receptor tyrosine kinases that play key roles in regulating cellular processes such as proliferation, differentiation, or cell survival (Bessman et al., 2014; Kovacs et al., 2015).

STAR★METHODS

Detailed methods are provided in the online version of this paper and include the following:

- KEY RESOURCES TABLE
- CONTACT FOR REAGENT AND RESOURCE SHARING
- EXPERIMENTAL MODEL AND SUBJECT DETAILS
- METHOD DETAILS
  - Phosphorylation assay
  - Preparation of a [^{13}C, ^{15}N]-labeled medium to label eukaryotic cells
  - ^{13}C, ^{15}N labeling of eukaryotic cells
  - Digestion of EGFR by Proteinase K enzyme
  - Membrane vesicle preparation
  - Preparation of [^{13}C, ^{15}N] A431 vesicles with EGF for NMR
  - Nanobody labeling and dSTORM and gSTED imaging
  - Cryo-electron microscopy
  - Mass spectrometry
  - Heatmaps of conformation-dependent amino acid distributions in EGFR
  - Solid-state NMR and DNP experiments
- QUANTIFICATION AND STATISTICAL ANALYSIS
  - Quantification of EGFR extracellular domain cleavage
  - Fluorescence intensity analysis of A431 membrane vesicles

SUPPLEMENTAL INFORMATION

Supplemental Information includes six figures and can be found with this article online at http://dx.doi.org/10.1016/j.cell.2016.10.038.

AUTHOR CONTRIBUTIONS

M.K., P.B.H., and M.B. designed experiments. M.K. and S.N. prepared isolated labeled EGFR membrane vesicles. M.K. and K.H. conducted ssNMR experiments. C.d.H. performed the phosphorylation assay. M.K. and C.d.H. performed confocal microscopy. P.J. and W.J.C.G. preformed EM. E.A.K, D.P.-C., P.J., and L.C.K. designed and performed the dSTORM and gSTED experiments. D.M. conducted DNP experiments and was supported by M.K. M.K. and R.D. prepared unlabeled A431 vesicles for MS experiments. S.D., S.L., and A.J.R.H. performed MS experiments. M.K., S.N., P.B.H, K.H., G.E.F., and M.B. analyzed data. M.K., P.B.H., and M.B. prepared the manuscript, and all authors edited it.

ACKNOWLEDGMENTS

We thank Willem Kegel and Markus Weingarth for helpful discussions and Johan van der Zwan for technical support. This work was funded in part by Netherlands Organization for Scientific Research (NWO) (grants 700.26.121 and 700.10.443 to M.B, STW12152 to P.B.H. and a VIDI grant 723.013.008 to SL) and iNEXT (project number 653706), a Horizon 2020 program of the European Union. In addition, S.v.D., S.L., and A.J.R.H. are supported by the project Proteins At Work (project 184.032.201), a program of the Netherlands Proteomics Centre financed by NWO as part of the National Roadmap Large-scale Research Facilities of the Netherlands. The NMR experiments were supported in part by uNMR-NL, an NWO-funded National Roadmap Large-Scale Facility of the Netherlands. We are indebted to Paul Tordo and Olivier Ouari (Marseille) for providing AMUPol.

Received: May 4, 2016
Revised: August 8, 2016
Accepted: October 20, 2016
Published: November 10, 2016

REFERENCES

Andronesi, O.C., Becker, S., Seidel, K., Heise, H., Young, H.S., and Baldus, M. (2005). Determination of membrane protein structure and dynamics by magic-angle-spinning solid-state NMR spectroscopy. J. Am. Chem. Soc. *127*, 12965–12974.

Arkhipov, A., Shan, Y., Das, R., Endres, N.F., Eastwood, M.P., Wemmer, D.E., Kuriyan, J., and Shaw, D.E. (2013). Architecture and membrane interactions of the EGF receptor. Cell *152*, 557–569.

Arkhipov, A., Shan, Y., Kim, E.T., and Shaw, D.E. (2014). Membrane interaction of bound ligands contributes to the negative binding cooperativity of the EGF receptor. PLoS Comput. Biol. *10*, e1003742.

Arteaga, C.L., and Engelman, J.A. (2014). ERBB receptors: from oncogene discovery to basic science to mechanism-based cancer therapeutics. Cancer Cell *25*, 282–303.

Baker, L.A., Daniëls, M., van der Cruijsen, E.A.W., Folkers, G.E., and Baldus, M. (2015). Efficient cellular solid-state NMR of membrane proteins by targeted protein labeling. J. Biomol. NMR *62*, 199–208.

Baldus, M., Petkova, A.T., Herzfeld, J., and Griffin, R.G. (1998). Cross polarization in the tilted frame: assignment and spectral simplification in heteronuclear spin systems. Mol. Physics *95*, 1197–1207.

Banci, L., Barbieri, L., Bertini, I., Luchinat, E., Secci, E., Zhao, Y., and Aricescu, A.R. (2013). Atomic-resolution monitoring of protein maturation in live human cells by NMR. Nat. Chem. Biol. *9*, 297–299.

Bessman, N.J., Freed, D.M., and Lemmon, M.A. (2014). Putting together structures of epidermal growth factor receptors. Curr. Opin. Struct. Biol. *29*, 95–101.

Chow, W.Y., Rajan, R., Muller, K.H., Reid, D.G., Skepper, J.N., Wong, W.C., Brooks, R.A., Green, M., Bihan, D., Farndale, R.W., et al. (2014). NMR spectroscopy of native and in vitro tissues implicates polyADP ribose in biomineralization. Science *344*, 742–746.

Coskun, Ü., Grzybek, M., Drechsel, D., and Simons, K. (2011). Regulation of human EGF receptor by lipids. Proc. Natl. Acad. Sci. USA *108*, 9044–9048.

Cox, J., and Mann, M. (2008). MaxQuant enables high peptide identification rates, individualized p.p.b.-range mass accuracies and proteome-wide protein quantification. Nat. Biotechnol. *26*, 1367–1372.

Dawson, J.P., Berger, M.B., Lin, C.-C., Schlessinger, J., Lemmon, M.A., and Ferguson, K.M. (2005). Epidermal growth factor receptor dimerization and activation require ligand-induced conformational changes in the dimer interface. Mol. Cell. Biol. *25*, 7734–7742.

Doerner, A., Scheck, R., and Schepartz, A. (2015). Growth Factor Identity Is Encoded by Discrete Coiled-Coil Rotamers in the EGFR Juxtamembrane Region. Chem. Biol. *22*, 776–784.

Edelstein, A., Amodaj, N., Hoover, K., Vale, R., and Stuurman, N. (2010). Computer control of microscopes using μManager. (Curr. Protoc. Mol. Biol.) Chapter 14, Unit14.20.

Endres, N.F., Das, R., Smith, A.W., Arkhipov, A., Kovacs, E., Huang, Y., Pelton, J.G., Shan, Y., Shaw, D.E., Wemmer, D.E., et al. (2013). Conformational coupling across the plasma membrane in activation of the EGF receptor. Cell *152*, 543–556.

Etzkorn, M., Seidel, K., Li, L., Martell, S., Geyer, M., Engelhard, M., and Baldus, M. (2010). Complex formation and light activation in membrane-embedded sensory rhodopsin II as seen by solid-state NMR spectroscopy. Structure *18*, 293–300.

Ferguson, K.M., Berger, M.B., Mendrola, J.M., Cho, H.S., Leahy, D.J., and Lemmon, M.A. (2003). EGF activates its receptor by removing interactions that autoinhibit ectodomain dimerization. Mol. Cell *11*, 507–517.

Frederick, K.K., Michaelis, V.K., Corzilius, B., Ong, T.-C., Jacavone, A.C., Griffin, R.G., and Lindquist, S. (2015). Sensitivity-enhanced NMR reveals alterations in protein structure by cellular milieus. Cell *163*, 620–628.

Frishman, D., and Argos, P. (1995). Knowledge-based protein secondary structure assignment. Proteins *23*, 566–579.

Garrett, T.P.J., McKern, N.M., Lou, M., Elleman, T.C., Adams, T.E., Lovrecz, G.O., Zhu, H.-J., Walker, F., Frenkel, M.J., Hoyne, P.A., et al. (2002). Crystal structure of a truncated epidermal growth factor receptor extracellular domain bound to transforming growth factor alpha. Cell *110*, 763–773.

Garrett, T.P.J., McKern, N.M., Lou, M., Elleman, T.C., Adams, T.E., Lovrecz, G.O., Kofler, M., Jorissen, R.N., Nice, E.C., Burgess, A.W., and Ward, C.W. (2003). The crystal structure of a truncated ErbB2 ectodomain reveals an active conformation, poised to interact with other ErbB receptors. Mol. Cell *11*, 495–505.

Gradmann, S., Ader, C., Heinrich, I., Nand, D., Dittmann, M., Cukkemane, A., van Dijk, M., Bonvin, A.M.J.J., Engelhard, M., and Baldus, M. (2012). Rapid prediction of multi-dimensional NMR data sets. J. Biomol. NMR *54*, 377–387.

Haigler, H., Ash, J.F., Singer, S.J., and Cohen, S. (1978). Visualization by fluorescence of the binding and internalization of epidermal growth factor in human carcinoma cells A-431. Proc. Natl. Acad. Sci. USA *75*, 3317–3321.

den Hartigh, J.C., van Bergen en Henegouwen, P.M., Verkleij, A.J., and Boonstra, J. (1992). The EGF receptor is an actin-binding protein. J. Cell Biol. *119*, 349–355.

Hoffman, D.B., Pearson, C.G., Yen, T.J., Howell, B.J., and Salmon, E.D. (2001). Microtubule-dependent changes in assembly of microtubule motor proteins and mitotic spindle checkpoint proteins at PtK1 kinetochores. Mol. Biol. Cell *12*, 1995–2009.

Hong, M., Zhang, Y., and Hu, F. (2012). Membrane protein structure and dynamics from NMR spectroscopy. Annu. Rev. Phys. Chem. *63*, 1–24.

Jura, N., Endres, N.F., Engel, K., Deindl, S., Das, R., Lamers, M.H., Wemmer, D.E., Zhang, X., and Kuriyan, J. (2009). Mechanism for activation of the EGF receptor catalytic domain by the juxtamembrane segment. Cell *137*, 1293–1307.

Kaplan, M., Cukkemane, A., van Zundert, G.C.P., Narasimhan, S., Daniëls, M., Mance, D., Waksman, G., Bonvin, A.M.J.J., Fronzes, R., Folkers, G.E., and Baldus, M. (2015). Probing a cell-embedded megadalton protein complex by DNP-supported solid-state NMR. Nat. Methods *12*, 649–652.

Kaszuba, K., Grzybek, M., Orłowski, A., Danne, R., Róg, T., Simons, K., Coskun, Ü., and Vattulainen, I. (2015). N-Glycosylation as determinant of epidermal growth factor receptor conformation in membranes. Proc. Natl. Acad. Sci. USA *112*, 4334–4339.

Kern, D., and Zuiderweg, E.R. (2003). The role of dynamics in allosteric regulation. Curr. Opin. Struct. Biol. *13*, 748–757.

Kerns, S.J., Agafonov, R.V., Cho, Y.-J., Pontiggia, F., Otten, R., Pachov, D.V., Kutter, S., Phung, L.A., Murphy, P.N., Thai, V., et al. (2015). The energy landscape of adenylate kinase during catalysis. Nat. Struct. Mol. Biol. *22*, 124–131.

Koers, E.J., van der Cruijsen, E.A.W., Rosay, M., Weingarth, M., Prokofyev, A., Sauvée, C., Ouari, O., van der Zwan, J., Pongs, O., Tordo, P., et al. (2014). NMR-based structural biology enhanced by dynamic nuclear polarization at high magnetic field. J. Biomol. NMR *60*, 157–168.

Kovacs, E., Zorn, J.A., Huang, Y., Barros, T., and Kuriyan, J. (2015). A structural perspective on the regulation of the epidermal growth factor receptor. Annu. Rev. Biochem. *84*, 739–764.

Kremer, J.R., Mastronarde, D.N., and McIntosh, J.R. (1996). Computer visualization of three-dimensional image data using IMOD. J. Struct. Biol. *116*, 71–76.

Liu, Y.C., Yen, H.Y., Chen, C.Y., and Chen, C.H. (2011). Sialylation and fucosylation of epidermal growth factor receptor suppress its dimerization and activation in lung cancer cells. Proc. Natl. Acad. Sci. USA *108*, 11332–11337.

Low-Nam, S.T., Lidke, K.A., Cutler, P.J., Roovers, R.C., van Bergen en Henegouwen, P.M., Wilson, B.S., and Lidke, D.S. (2011). ErbB1 dimerization is promoted by domain co-confinement and stabilized by ligand binding. Nat. Struct. Mol. Biol. *18*, 1244–1249.

Lu, C., Mi, L.-Z., Grey, M.J., Zhu, J., Graef, E., Yokoyama, S., and Springer, T.A. (2010). Structural evidence for loose linkage between ligand binding and kinase activation in the epidermal growth factor receptor. Mol. Cell. Biol. *30*, 5432–5443.

Matsushita, C., Tamagaki, H., Miyazawa, Y., Aimoto, S., Smith, S.O., and Sato, T. (2013). Transmembrane helix orientation influences membrane binding of the intracellular juxtamembrane domain in Neu receptor peptides. Proc. Natl. Acad. Sci. USA *110*, 1646–1651.

Mikhaylova, M., Cloin, B.M.C., Finan, K., van den Berg, R., Teeuw, J., Kijanka, M.M., Sokolowski, M., Katrukha, E.A., Maidorn, M., Opazo, F., et al. (2015). Resolving bundled microtubules using anti-tubulin nanobodies. Nat. Commun. *6*, 7933.

Miljan, E.A., and Bremer, E.G. (2002). Regulation of growth factor receptors by gangliosides. Sci. STKE *2002*, re15.

Morris, G.A., and Freeman, R. (1979). Enhancement of Nuclear Magnetic-Resonance Signals by Polarization Transfer. J. Am. Chem. Soc. *101*, 760–762.

Ni, Q.Z., Daviso, E., Can, T.V., Markhasin, E., Jawla, S.K., Swager, T.M., Temkin, R.J., Herzfeld, J., and Griffin, R.G. (2013). High frequency dynamic nuclear polarization. Acc. Chem. Res. *46*, 1933–1941.

Nygaard, R., Zou, Y., Dror, R.O., Mildorf, T.J., Arlow, D.H., Manglik, A., Pan, A.C., Liu, C.W., Fung, J.J., Bokoch, M.P., et al. (2013). The dynamic process of β(2)-adrenergic receptor activation. Cell *152*, 532–542.

Ogiso, H., Ishitani, R., Nureki, O., Fukai, S., Yamanaka, M., Kim, J.-H., Saito, K., Sakamoto, A., Inoue, M., Shirouzu, M., and Yokoyama, S. (2002). Crystal structure of the complex of human epidermal growth factor and receptor extracellular domains. Cell *110*, 775–787.

Pines, A., Gibby, M.G., and Waugh, J.S. (1973). Proton-Enhanced NMR of Dilute Spins in Solids. J. Chem. Phys. *59*, 15–19.

Renault, M., Tommassen-van Boxtel, R., Bos, M.P., Post, J.A., Tommassen, J., and Baldus, M. (2012). Cellular solid-state nuclear magnetic resonance spectroscopy. Proc. Natl. Acad. Sci. USA *109*, 4863–4868.

Santoni, V., Molloy, M., and Rabilloud, T. (2000). Membrane proteins and proteomics: un amour impossible? Electrophoresis *21*, 1054–1070.

Sauvée, C., Rosay, M., Casano, G., Aussenac, F., Weber, R.T., Ouari, O., and Tordo, P. (2013). Highly efficient, water-soluble polarizing agents for dynamic nuclear polarization at high frequency. Angew. Chem. Int. Ed. Engl. *52*, 10858–10861.

Schneider, R., Seidel, K., Etzkorn, M., Lange, A., Becker, S., and Baldus, M. (2010). Probing molecular motion by double-quantum (13C,13C) solid-state NMR spectroscopy: application to ubiquitin. J. Am. Chem. Soc. *132*, 223–233.

Sengupta, P., Bosis, E., Nachliel, E., Gutman, M., Smith, S.O., Mihályné, G., Zaitseva, I., and McLaughlin, S. (2009). EGFR juxtamembrane domain, membranes, and calmodulin: kinetics of their interaction. Biophys. J. *96*, 4887–4895.

Serber, Z., Keatinge-Clay, A.T., Ledwidge, R., Kelly, A.E., Miller, S.M., and Dötsch, V. (2001). High-resolution macromolecular NMR spectroscopy inside living cells. J. Am. Chem. Soc. *123*, 2446–2447.

Shaka, A.J., Barker, P.B., and Freeman, R. (1985). Computer-optimized decoupling scheme for wideband applications and low-level operation. J. Magn. Reson. *64*, 547–552.

Smith, M.J., Marshall, C.B., Theillet, F.-X., Binolfi, A., Selenko, P., and Ikura, M. (2015). Real-time NMR monitoring of biological activities in complex physiological environments. Curr. Opin. Struct. Biol. *32*, 39–47.

Stamos, J., Sliwkowski, M.X., and Eigenbrot, C. (2002). Structure of the epidermal growth factor receptor kinase domain alone and in complex with a 4-anilinoquinazoline inhibitor. J. Biol. Chem. *277*, 46265–46272.

Tebbutt, N., Pedersen, M.W., and Johns, T.G. (2013). Targeting the ERBB family in cancer: couples therapy. Nat. Rev. Cancer *13*, 663–673.

Valley, C.C., Arndt-Jovin, D.J., Karedla, N., Steinkamp, M.P., Chizhik, A.I., Hlavacek, W.S., Wilson, B.S., Lidke, K.A., and Lidke, D.S. (2015). Enhanced dimerization drives ligand-independent activity of mutant epidermal growth factor receptor in lung cancer. Mol. Biol. Cell *26*, 4087–4099.

Wang, Y., and Jardetzky, O. (2002). Probability-based protein secondary structure identification using combined NMR chemical-shift data. Protein Sci. *11*, 852–861.

Weingarth, M., Demco, D.E., Bodenhausen, G., and Tekely, P. (2009). Improved magnetization transfer in solid-state NMR with fast magic angle spinning. Chem. Phys. Lett. *469*, 342–348.

Whitson, K.B., Whitson, S.R., Red-Brewer, M.L., McCoy, A.J., Vitali, A.A., Walker, F., Johns, T.G., Beth, A.H., and Staros, J.V. (2005). Functional effects of glycosylation at Asn-579 of the epidermal growth factor receptor. Biochemistry *44*, 14920–14931.

Yarden, Y. (2001). The EGFR family and its ligands in human cancer. signalling mechanisms and therapeutic opportunities. Eur. J. Cancer *37*(*Suppl 4*), S3–S8.

Ziomkiewicz, I., Loman, A., Klement, R., Fritsch, C., Klymchenko, A.S., Bunt, G., Jovin, T.M., and Arndt-Jovin, D.J. (2013). Dynamic conformational transitions of the EGF receptor in living mammalian cells determined by FRET and fluorescence lifetime imaging microscopy. Cytometry A *83*, 794–805.

STAR★METHODS

KEY RESOURCES TABLE

REAGENT or RESOURCE	SOURCE	IDENTIFIER
Antibodies		
Rabbit polyclonal anti-phosphoEGFR (Y1068)	Cell Signaling Technology	Cat#2234S
Rabbit monoclonal anti-EGFR (C74B9)	Cell Signaling Technology	Cat#2646S
Mouse anti-Actin (clone C4)	MP Biochemicals	Cat#691001; RRID: AB_2336056
Goat anti-mouse700	Li-Cor	Cat#926-68170; RRID: AB_10956589
Goat anti-rabbit800	Li-Cor	Cat#925-32211
Chemicals, Peptides, and Recombinant Proteins		
[^{13}C, ^{15}N] algal amino acids mixture	Cortecnet	Cat#CCN070P1
[^{13}C] L-Methionine	Cambridge Isotope Laboratories	Cat#CLM-893-H-PK
[^{13}C] L-Phenylalanine	Cambridge Isotope Laboratories	Cat#CLM-2250-H-PK
[^{15}N] L-Threonine	Cambridge Isotope Laboratories	Cat#NLM-742-PK
[^{15}N] L-Leucine	Cambridge Isotope Laboratories	Cat#NLM-142-PK
EGF	R&D Systems	Cat#236-EG-01M
EGF-A488	ThermoFisher Scientific	Cat#E-13345
AMUpol	Sauvée et al., 2013	N/A
Experimental Models: Cell Lines		
Human: A431	ATCC	Cat#CRL-1555; RIDD: CVCL-0037
Mouse: NIH 3T3 clone 2.2	ATCC	Cat#CRL-1658; RRID: CVCL-0594
Software and Algorithms		
DoM_Utrecht	Mikhaylova et al., 2015	https://github.com/ekatrukha/DoM_Utrecht
Topspin	Bruker Biospin	N/A
Sparky	T. D. Goddard and D. G. Kneller, SPARKY 3, University of California, San Francisco	https://www.cgl.ucsf.edu/home/sparky/
FANDAS	Gradmann et al., 2012	N/A
Odyssey Application Software 2.0	Li-Cor	N/A

CONTACT FOR REAGENT AND RESOURCE SHARING

Further information and requests for reagents may be directed to Paul van Bergen en Henegouwen (p.vanbergen@uu.nl).

EXPERIMENTAL MODEL AND SUBJECT DETAILS

A431 cells obtained from ATCC (CRL-1555, LGC Standards, Germany) and EGFR negative cells NIH 3T3 clone 2.2 murine fibroblasts were cultured in Dulbecco's modified eagle's medium (DMEM: GIBCO, invitrogen, Paisley, UK) containing 10% (v/v) fetal calf serum (FCS), L- glutamine, penicillin and streptomycin at 37°C with an atmosphere containing 5% CO_2.

METHOD DETAILS

Phosphorylation assay

Phosphorylation of EGFR was induced either by adding 8 nM EGF to the cells in medium before membrane vesicles were prepared or to membrane vesicles in a phosphorylation buffer for 10 min at 37°C. Proteins were separated by SDS-PAGE and blotted onto PVDF-membrane. The membrane was incubated with R-α-phosphoEGFR (Y1068) (Cell Signaling Technology, Danvers, Massachusetts) and M-α-Actin followed by G-α-R800 (Li-Cor) and G-α-mouse700 (Li-Cor). To detect EGFR the blot was first stripped with stripping buffer and then blocked and incubated with R-α-EGFR (C74B9, Cell signaling technology)) followed by G-α-R800. The detection was performed with the Odyssey imaging system (Li-COR) and bands were quantified using Odyssey software.

Preparation of a [^{13}C, ^{15}N]-labeled medium to label eukaryotic cells

For isotope labeling, we adapted published procedures using a combination of dialyzed fetal calf serum and labeled amino acid mixtures obtained from algae extracts to produce a [^{13}C, ^{15}N] enriched medium. 1 L of DMEM without amino acids was supplemented with 2 g/L glucose and 1g of a [^{13}C, ^{15}N] algal amino-acid mixture (Cortecnet). Due to the absence of certain amino acids in this mixture, unlabeled Trp (16 mg/L), Cys (62 mg/L) and Gln (2 mM) were added. In addition, 10% of dialyzed fetal calf serum was added to the medium. 1 g of labeled algal mixture contained the following amino acids: ASX: 8.8%, THR: 3.2%, SER: 4.6%, GLU: 8.2%, PRO: 4.0%, GLY: 8.3%, ALA: 11.9%, VAL: 7.0%, MET: 2.0%, ILE: 6.0%, LEU: 12.2%, TYR: 3.9%, PHE: 5.4%, HIS: 1.2%, LYS: 5.8%, TRP: 0.0%, ARG: 5.9%, CYS: 0.0%.

^{13}C, ^{15}N labeling of eukaryotic cells

A431 cells were cultured in the labeled medium described above on Corning cell culture dishes (150 mm x 25 mm). Cells cultured in the first week (2-3 passages) in the labeled medium were not used to prepare the samples to ensure full incorporation of labeled substance in the cells. Once the plates were ~80%–90% confluent, cells were incubated with PBS containing 2 mM EGTA at 37°C for 15 min, after which they were scraped. Subsequently, cells were spun at 500xg for 10 min at 4°C. The cell pellet was resuspended in PBS and spun again at 500xg for 10 min at 4°C and used to prepare the membrane vesicles as described below. Approximately 20 plates (150 mm x 25 mm) were used to fill a 3.2 mm rotor with [^{13}C, ^{15}N] labeled A431 membrane vesicles.

Digestion of EGFR by Proteinase K enzyme

Freshly prepared A431 membrane vesicles were incubated with 200 μg/mL of Proteinase K for 15 min on ice. Proteinase K was inactivated by diluting 2 nM PMSF in 1:1 ratio in the digestion mixture. The proteins were separated by SDS-PAGE and blotted onto PVDF membrane. The membrane was incubated overnight with R-α-EGFR (C74B9, Cell signaling technology) and M-α-Actin. The protein quantities were determined by incubation with G-α-R800 (Li-Cor) and G-α-mouse700 (Li-Cor), followed by detection on the Odyssey imaging system (Li-Cor).

Membrane vesicle preparation

Cells were re-suspended with homogenization buffer (10 mM Tris pH 7.4, 250 mM sucrose, 1 mM EDTA. Phosphatase inhibitors (100 μM sodium-orthovanadate) and protease inhibitors (Complete, Roche) were added freshly and cells were vesiculated by passing them 10 times through a syringe (21 gx1.5; 0.2x40mm). Subsequently, cells were spun at 1000xg at 4°C for 10 min to remove unbroken cells, nuclei and cell debris from the supernatant. This was repeated until no pellet was visible anymore. The supernatant was subsequently spun at 150,000xg for 30 min at 4°C to collect membrane vesicles. Vesicles were resuspended in 10 mM HEPES pH 7.4, supplemented with protease and phosphatase inhibitors.

Preparation of [^{13}C, ^{15}N] A431 vesicles with EGF for NMR

Isolated A431 membrane vesicles were spun down at 124,000x*g* for 25 min at 4°C, and the pellet was resuspended in phosphorylation buffer (20 mM HEPES pH 7, 10 mM $MgCl_2$, 3 mM $MnCl_2$, 1 mM DTT, with protease and phosphatase inhibitors. To this buffer, 1 mM ATP was added. The vesicles were incubated with 8 nM EGF at 37°C for 10 min. Subsequently, the vesicles were washed three times with 10 mM HEPES pH 7.4 buffer containing protease and phosphatase inhibitors. For DNP samples, the sample was washed once with 10 mM HEPES pH 7.4 (containing protease and phosphatase inhibitors) and then two times with DNP buffer: 20 μl AMUPol[5] (in D_2O), 20 μl H_2O, 20 μl D_2O, 40 mg glycerol-d8 (equivalent to 30 ul) and 10 μl 100 mM HEPES. For each washing step, 50 μl of the buffer was used.

Nanobody labeling and dSTORM and gSTED imaging

Vesicles derived from A431 cells were labeled in suspension with 10 nM anti-EGFR (7D12) nanobodies conjugated to Alexa647, 8 nM EGF conjugated to Alexa488 and 10 μM DiI (1,1'-Dioctadecyl-3,3,3′,3′-Tetramethylindocarbocyanine Perchlorate) for 1 hr at 4°C. Non-bound ligands were removed by centrifugation at 75,000xg for 40 min and vesicles were attached to glass slides for microscopical analysis.

dSTORM microscopy was performed on a Nikon Ti microscope equipped with a 100x Apo TIRF oil objective (NA. 1.49), a Perfect Focus System and an additional 2.5x Optovar to achieve an effective pixel size of 64 nm (Mikhaylova et al., 2015). Evanescent laser illumination was achieved using a custom illumination pathway with a 15 mW 405 nm diode laser (Power Technology) and a 40 mW 640 nm diode laser (Power Technology). Fluorescence was detected using a water-cooled Andor DU-897D EMCDD camera and ET series Cy5 filter (Chroma Technology). All components were controlled by μmanager software (Edelstein et al., 2010). For dSTORM imaging of Alexa Fluor 647, the sample was continuously illuminated with 640 nm. In addition, the sample was illuminated with 405 nm light at increasing intensity to keep the number of fluorophores in the fluorescent state constant. Between 5000 and 10000 frames were recorded per acquisition with exposure time of 40 ms. Purified vesicles from A431 (EGFR-positive) and 3T3 fibroblasts (EGFR negative) were incubated with 10 nM of anti-EGFR or non-specific nanobodies fused to Alexa647 for one hour at 4°C. Four flow chambers with an approximate volume of 5 μL each were made with stripes of double-sided tape between a plasma-cleaned 22x22 mm coverslip and the microscope slide. These chambers were filled with four consecutive 10 times dilutions of labeled vesicles and incubated for 5 min at RT. The chamber was washed with 25 μL of imaging buffer to remove

non-attached vesicles and sealed using vacuum grease. The composition of the imaging buffer was 100 mM MEA, 5% w/v glucose, 700 μg/ml glucose oxidase and 40 μg/ml catalase in PBS buffer. The dilution containing optimal density of vesicles on the coverslip was chosen for the imaging (~20-30 vesicles per 100 μm^2). The signals from 3T3 fibroblasts vesicles labeled with anti-EGFR nanobody and A431 vesicles labeled with non-specific nanobody were not distinguishable from the noise. Analysis of the dSTORM localization and rendering was performed using a custom written ImageJ plugin for the single-molecule localization (https://github.com/ekatrukha/DoM_Utrecht). Each spot was fitted with asymmetric two-dimensional Gaussian PSF and only fits with a calculated width within ± 30% of the measured PSF's SD were accepted. Localizations within one pixel distance in a number of successive frames were considered to arise from the same molecule. In this case the weighted mean was calculated for each coordinate, where weights were equal to inverse squared localization errors. The resulting table with molecule coordinates was used to render the final localization image with 5 nm pixel size. Each molecule was plotted as a 2D Gaussian of the integrated intensity equal to one and with SD in *x* and *y* equal to the localization precision. The noise arising from non-specific localization was suppressed using local density based filtering. Only particles having more than 150 neighbors in the circle of 250 nm radius were kept in the reconstruction.

Gated STED imaging of A431 vesicles was performed with a Leica TCS SP8 STED 3X microscope using HC PL APO 100x/1.4 oil STED WHITE objective. Alexa488 EGF was excited with the 488 nm wavelength of pulsed white laser (80MHz) and depleted with CW 592 nm STED laser. DiI was excited with 561 nm line and depleted with CW 660 nm line. Alexa647 conjugated anti-EGFR nanobody was imaged with 633 nm excitation with white laser and depleted with 775 nm pulsed laser. Images were acquired in 2D STED mode with vortex phase mask. Depletion laser power was equal to 10%–30% of maximum power and we used an internal Leica GaAsP HyD hybrid detector with a time gate of $0.3 \leq tg \leq 6$ ns. Confocal three color imaging was performed on the same setup using the same white laser excitation and emission settings from LAS X controlling software library.

Cryo-electron microscopy

For the preparation of thin vitrified specimens of the A431 vesicles, a 3 ul drop of sample was placed on the surface of a glow discharged Quantifoil micromachined holey carbon (R 2/2) TEM grid (Quantifoil Micro Tools GmbH, Jena, Germany) held by the Vitrobot mark IV tweezer (FEI, Eindhoven, the Netherlands). Before introducing the sample into the Vitrobot, the environmental chamber of the Vitrobot was equilibrated at room temperature (22°C) and humidity was set at 100%. Blotting conditions were chosen so that a 10-500 nm liquid specimen film spanning R 2/2 μm holes of the QF were formed when excess sample was removed by the blotting filter paper in the Vitrobot. The specimen was released and fell through the opening shutter and into liquid ethane at its freezing point, where the thin specimen films were vitrified. The vitreous specimen was transferred under liquid nitrogen into a Gatan 626 single tilt liquid nitrogen cryo holder (Gatan GmbH, Munich, Germany) and into a Tecnai20 LaB6 electron microscope (FEI, Eindhoven, the Netherlands), where the specimen temperature was maintained below −165°C. An Eagle 4k × 4k CCD camera (FEI, Eindhoven, the Netherlands) was used under normal and low-dose conditions to record micrographs of the vesicles, which was done in Tif format with a nominal under focus of 3 μm. Vesicle diameter was measured using the IMOD software package (Kremer et al., 1996).

Mass spectrometry

A431 vesicles and cells were lysed in 50mM ammonium bicarbonate, 1% SDC, 10mM TCEP, 100mM TRIS, 40mM chloroacetamide and complete protease inhibitor cocktail (Roche) and boiled for 5 min at 95°C. The supernatant was diluted 10 times and digested overnight using LysC (1:75) and trypsin (1:50). SDC was removed by acidifying the samples with formic acid and spinning down. The supernatant was desalted using C18 SepPak (Waters) cartridges, vacuum-dried and stored at −80°C for further analysis. Peptide mixtures were reconstituted in 10% formic acid and 1μg of protein digest of each sample was analyzed by nano-LC-MS/MS on an Orbitrap Q-Exactive plus (ThermoFisher Scientific, Bremen). The digest was trapped on an in-house made trap column (Reprosil pur C18, dr maisch, 100 μm x 2 cm, 3 μm) by loading for 10 min with A (A: 0.1% formic acid) and separated on an analytical column (Poroshell 120 EC C18, Agilent Technologies, 50 μm x 50 cm, 2.7 μm) using a 2 hr linear gradient from 13% to 40% B (B: 0.1% formic acid, 80% ACN). During each scan cycle, the 10 most intense peptide precursors were selected for higher-energy collisional dissociation (HCD). Raw data files were processed with MaxQuant version 1.5.3.30. The data were searched against the Human UniProt database (February 2016, 151.869 entries). A false discovery rate was set to 1% at protein and peptide level. Peptide intensities were normalized to total peptide intensities in each LC-MS run. For relative quantification, intensities of all unique and razor peptides of a protein were summed up (Cox and Mann, 2008).

Heatmaps of conformation-dependent amino acid distributions in EGFR

The available structures were first split according to individual domains (DI-IV, TM, KD, and CT). Domain segments that were elusive from the available structures were built in random-coil conformation using PyMol. Secondary structure assignments were made for these structures by supplying the .pdb files to the software: STRuctural IDEntification (STRIDE, Frishman and Argos, 1995), which uses the phi and psi angles of the residues to assign secondary structures. The secondary structure assignments were sorted into three categories based on their similarity: α-helix (simplified from a-helix and 3_{10} helix), β sheet (simplified from strand and bridge) and random coil (for turn and coil). These data were subsequently used to calculate the amino acid distribution per secondary structure over the whole protein.

Solid-state NMR and DNP experiments

NMR experiments were conducted using a standard-bore 700 MHz as well as wide-bore 800 MHz/ 527 GHz DNP and 400 MHz/263 GHz DNP systems (Bruker Biospin). We filled fully [^{13}C, ^{15}N] or MFTL labeled A431 membrane vesicles obtained from around 20 (150 mm x 25 mm) plates into standard 3.2 mm rotors. For all DNP measurements, samples were cooled down to 100°K using 3.2 mm sapphire rotors. DNP samples were prepared using AMUpol (Sauvée et al., 2013) and buffers as described above. The DNP enhancement was measured by overlaying HC and HN CP/MAS spectra recorded with and without microwave irradiation. Two and three-dimensional NC correlation spectra were recorded using SPECIFIC-CP N-^{13}C transfers (Baldus et al., 1998). Homo-nuclear (^{13}C,^{13}C) transfers were established using PARIS (Weingarth et al., 2009) or spin-diffusion mixing blocks. ^{1}H decoupling using SPINAL64 was employed during evolution and detection periods except in HC HETCOR (Figure S4) where GARP (Shaka et al., 1985) decoupling was employed at 10 KHz. Below the processing parameters for the NMR experiments displayed as main or supplemental Figures are given.

Processing parameters of DQSQ in Figure 4 A-F

Field strength	CP time [μs]	SPC5 mixing time [ms]	Temperature [K]	MAS [kHz]
700 MHz	500	2.3	285	9

The DQSQ CC 2D datasets (with and without EGF) in Figure 4 were acquired using 110 t_1 points with a spectral window of 46656.176 Hz in t_1. The spectra were processed using an EM function, line broadening 100 Hz in t_2 and t_1 and with 2K and 1K zero filling in t_2 and t_1 respectively, with 8 coefficients linear prediction in t_1. Note that the experiment with EGF was multiplied by factor 1.4 to compensate for the sample amount compared to the sample without EGF.

Processing parameters of NCOCX data in Figure 5B, D and E

Spectrum	HN, CP time [μs]	SPECIFIC CP mixing [ms]	PDSD mixing time [ms]	Temperature [K]	MAS [kHz]	Total acquisition time (days)
NCOCX 400 MHz DNP, With EGF	350	4.6	20	100	8	~3.5
NCOCX 400 MHz DNP, No EGF	200	4.8	20	100	8	~3.5

The NCOCX experiments in Figure 5 (400 MHz DNP) were acquired using 8 points in t_1 and 13 points in t_2 with spectral width of 3012.048 Hz and 1620.745 Hz in t_2 and t_1 respectively. The spectra were processed using a squared sine bell function 3 in t_3, t_2 and t_1 with 4k zero filling in t_3. In t_2 and t_1 128 points of zero filling were used.

Processing parameters of ^{15}N-edited CC spectrum in Figure 5C

Spectrum	HN, CP time [μs]	SPECIFIC CP mixing [ms]	PDSD mixing time [ms]	Temperature [K]	MAS [kHz]	Total acquisition time (days)
N-edited CC 400 MHz DNP, With EGF	350	4.6	20	100	8	~2.5
N-edited CC 400 MHz DNP, No EGF	350	4.8	20	100	8	~2.5

The ^{15}N-edited CC experiments in Figure 5C were acquired using 50 points in t_1 with spectral width of 12569.131 Hz in t_1. The spectra were processed using a squared sine bell function 2 in t_2 and t_1 with 2k zero filling in t_2. In t_1 128 points of zero filling were used.

Processing parameters of DQSQ data in Figure S1 C

Field strength	CP time [μs]	SPC5 mixing time [ms]	Temperature [K]	MAS [kHz]
700 MHz	500	2.3	253 K	9

The DQSQ CC 2D datasets in Figure S1C were acquired using 110 t_1 points with a spectral window of 46656.176 Hz in t_1. The spectrum was processed using EM function, line broadening 100 Hz in t_2 and t_1 and with 2k and 1K zero filling in t_2 and t_1 respectively, with 8 coefficients linear prediction in t_1.

Processing parameters of CC PARIS in Figure S2				
Field strength	CP time [μs]	PARIS mixing time [ms]	Temperature [K]	MAS [kHz]
700 MHz	500	30	253	9

The PARIS CC 2D dataset in Figure S2 was acquired using 221 t_1 points with a spectral window of 36982.246 Hz in t_1. The spectrum was processed using EM function with line broadening 100 Hz in both t_1 and t_2. 1k and 2k zero filling was used in both t_1 and t_2 respectively, with 4 linear prediction coefficients in t_1.

Processing parameters of HC HETCOR in Figure S4		
Field strength	Temperature [K]	MAS [kHz]
700 MHz	285 K	9

The HC HETCOR 2D dataset in Figure S4 was acquired using 92 t_1 points with a spectral window of 7142.86 Hz in t_1. The spectrum was processed using squared sine function (SSB = 2) in both t_1 and t_2. 1k and 2k zero filling was used in both t_1 and t_2 respectively, with 40 linear prediction coefficients in t_1.

Processing parameters of NCOCX data in Figure S6B					
Field strength	HN, CP time [μs]	SPECIFIC CP time [ms]	PDSD mixing [ms]	Temperature [K]	MAS [kHz]
NCOCX 800 MHz DNP, With EGF	400	3.6	20	100	8
NCOCX 800 MHz DNP, No EGF	350	4.0	20	100	8

The NCOCX experiments in Figure S6B (800 MHz DNP) were acquired using 15 t_1 points with a spectral width of 3333.33 Hz in t_1. The spectra were processed using squared sine function 2.5 in both t_1 and t_2 with 4k and 1k zero filling points in t_2 and t_1 respectively.

QUANTIFICATION AND STATISTICAL ANALYSIS

Quantification of EGFR extracellular domain cleavage

Intensity of EGFR- and actin-positive bands on western blot were quantified using the Odyssey Application software. The total amount of EGFR is corrected for the loading control. The percentage of EGFR extracellular domain cleavage was calculated as a product of the sum of full-length EGFR and the EGFR degradation product.

Fluorescence intensity analysis of A431 membrane vesicles

The measurements of integrated fluorescence intensity without background were performed similar to method described previously (Hoffman et al., 2001) using custom written ImageJ plugin DoM_Utrecht (https://github.com/ekatrukha/DoM_Utrecht). We counted raw integrated intensity IR of squared 13 × 13 pixel region of area SR that was centered on the maximum intensity pixel of a fluorescent spot. The raw integrated intensity of background IB was equal to integrated counts of 14 × 14 pixel region of area SB minus IR. The final integrated fluorescence intensity (without background) IF was equal to:

$$I_F = I_R - I_B \frac{S_R}{S_B}$$

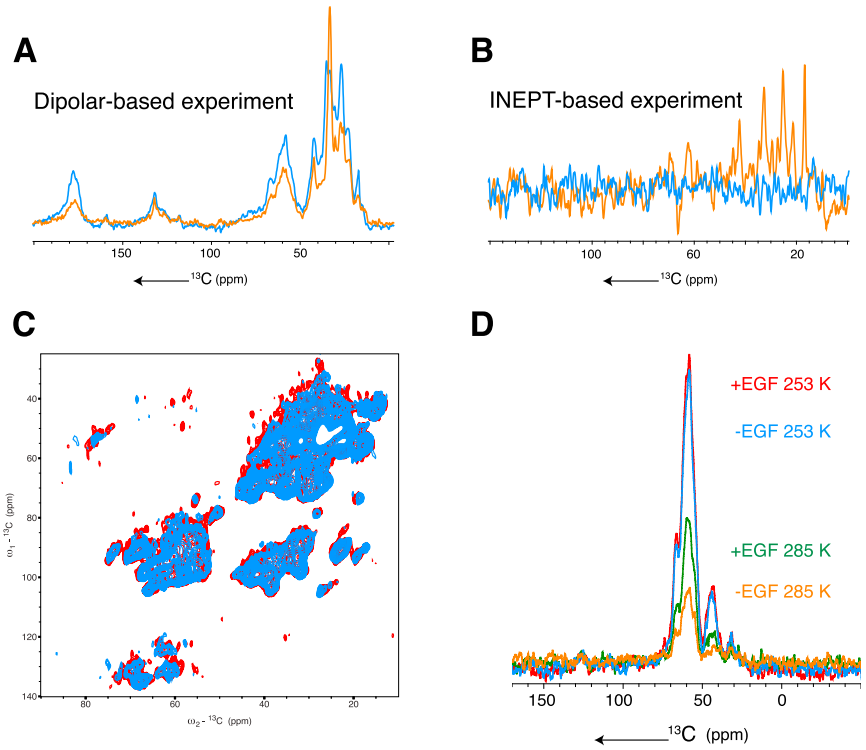

Figure S1. Temperature Dependence of One- and Two-Dimensional ssNMR Experiments Using [^{13}C, ^{15}N]-Labeled A431 Plasma Membrane Vesicles with and without EGF, Related to Figure 4

(A) ^{13}C CP (cross polarization, which probes the rigid parts of the sample (Pines et al., 1973)) experiment of [^{13}C, ^{15}N]-labeled A431 plasma membrane vesicles without EFG at 253 K (blue) and 285 K (orange).

(B) INEPT-based (See (Morris and Freeman, 1979) experiment, to probe the mobile parts of the sample of [^{13}C, ^{15}N]-labeled A431 plasma membrane vesicles without EFG at 253 K (blue) and 285 K (orange).

(C) 2D ^{13}C,^{13}C) double-quantum / single-quantum experiment (DQSQ) with (red) and without (blue) EGF performed at 253 K.

(D) First increment of 2D NCa of [^{13}C, ^{15}N]-labeled A431 plasma membrane vesicles without EGF (blue at 253 K and orange at 285 K) and with EGF (red at 253 K and green at 285 K).

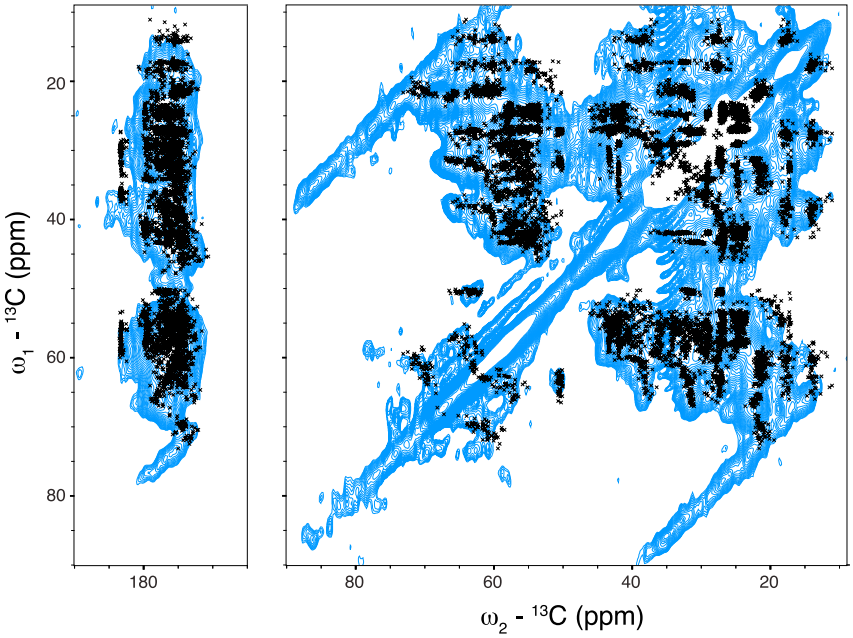

Figure S2. Comparison of ssNMR Spectra of [^{13}C, ^{15}N]-Labeled A431 Membrane Vesicles at Low Temperatures to EGFR Chemical-Shift Predictions, Related to Figure 4

The 2D (^{13}C,^{13}C) PARIS experiment was performed at 253 K. Black crosses represent FANDAS (Gradmann et al., 2012) predictions of EGFR based on the different available structures and assuming random-coil chemical shifts for the C-terminal region (CT). Note that the peaks at ~70 ppm are stemming from lipids. As mentioned in the section Materials and Methods, EGFR samples were prepared using unlabeled Glutamine, Tryptophan and Cysteine amino acids and, correspondingly, were not included in the FANDAS correlation map. FANDAS predictions were made based on the following structures: 1NQL (Extracellular inactive), 2M20 (Transmembrane domain), 2M20 (Juxtamembrane), 1M14 (Kinase domain), 1M14 (part of the C-terminal tail).

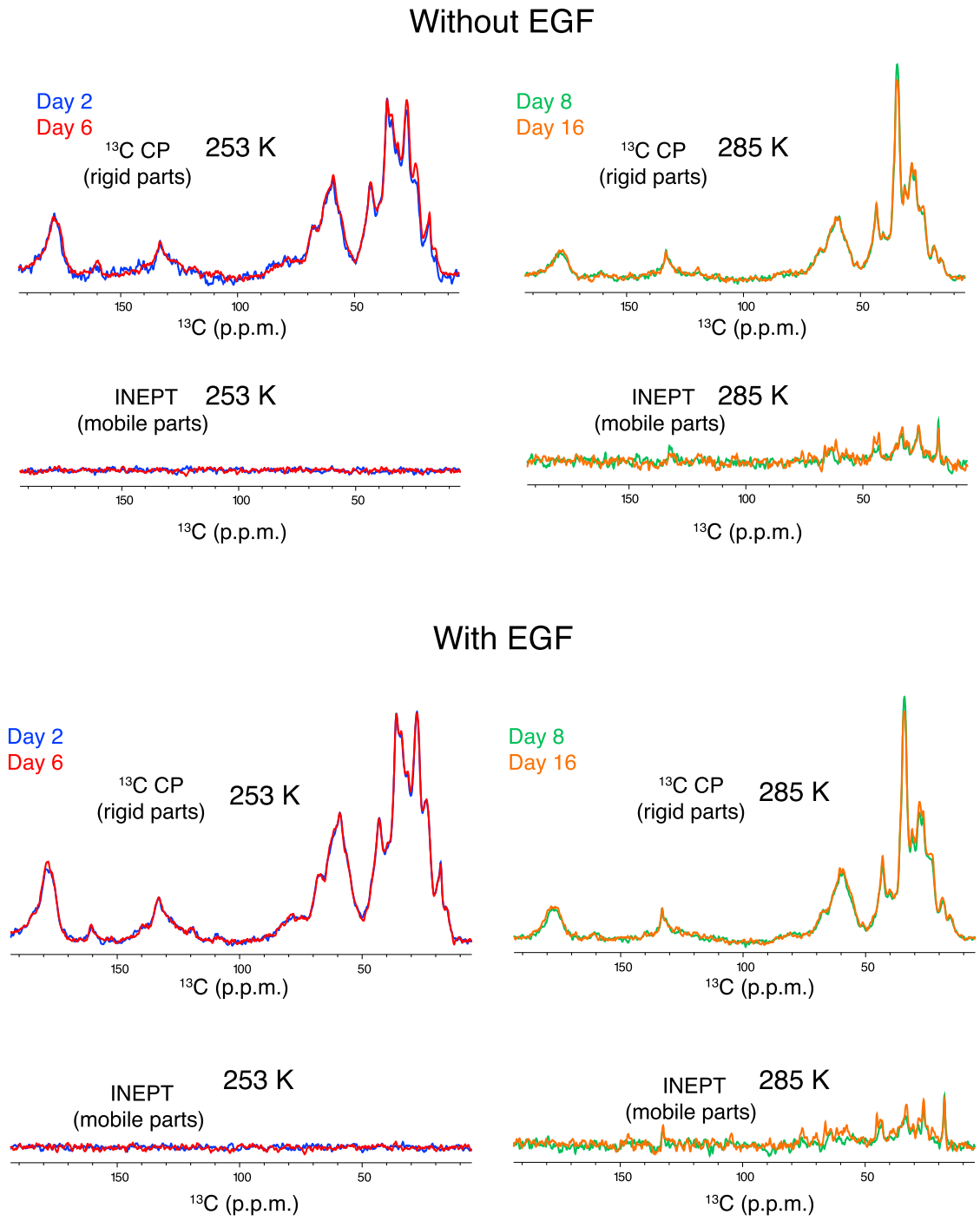

Figure S3. ssNMR Signal Patterns for Extended Measurement Periods, Related to Figure 4

1D ^{13}C CP and INEPT on [^{13}C, ^{15}N]-labeled A431 vesicles with and without EGF performed during the course of 2D experiments. At the end of measurements (day 16), both samples showed the same profile as in the beginning of the measurements. Data were recorded on a 700 MHz NMR instrument.

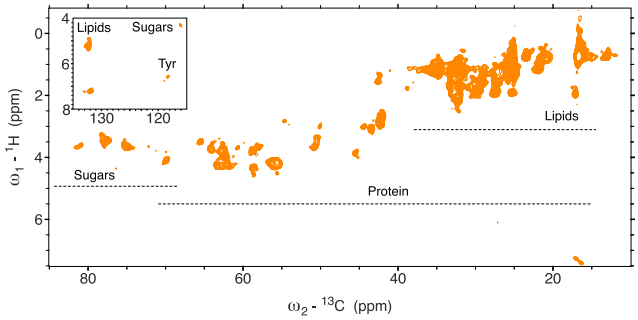

Figure S4. Mobile Molecules Appear at Higher Temperature in 2D ssNMR Data, Related to Figure 4

2D INEPT experiment (See Andronesi et al., 2005) of [^{13}C, ^{15}N]-labeled A431 membrane vesicles without EGF performed at 285 K showing mobile molecular components.

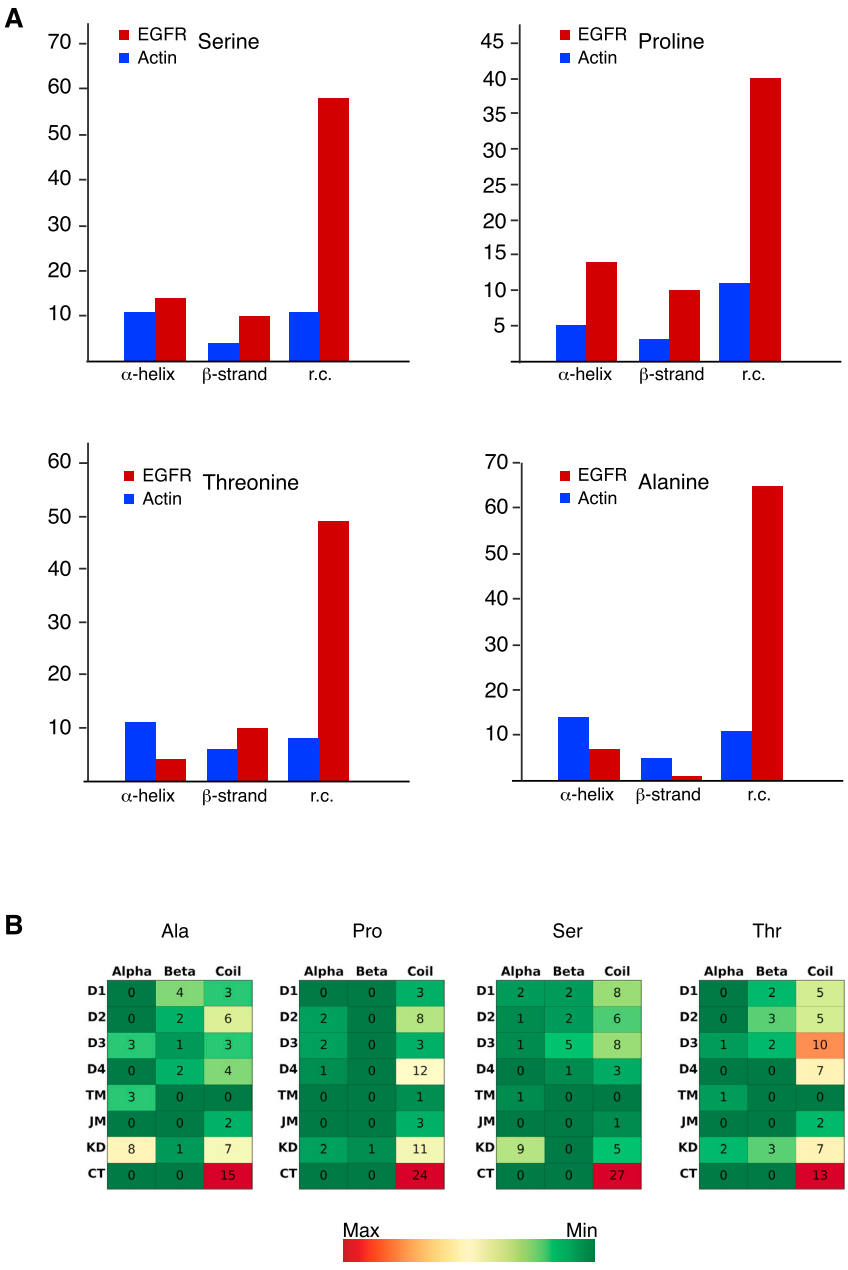

Figure S5. Secondary-Structure Analysis of EGFR, Actin, and EGFR Domains, Related to Figures 4 and 5

(A) Comparison of the distribution of Ser, Thr, Pro and Ala residue in different secondary structures between EGFR (red) and Actin (blue). The y axis represents the number of each amino acid in the correspondent secondary structure.

(B) Heatmaps of the distribution of Ala, Pro, Ser and Thr residues in EGFR for the three secondary structure elements (α-helix, β strand and random coil). Red and green stand for the highest and lowest numbers of occurrence, respectively.

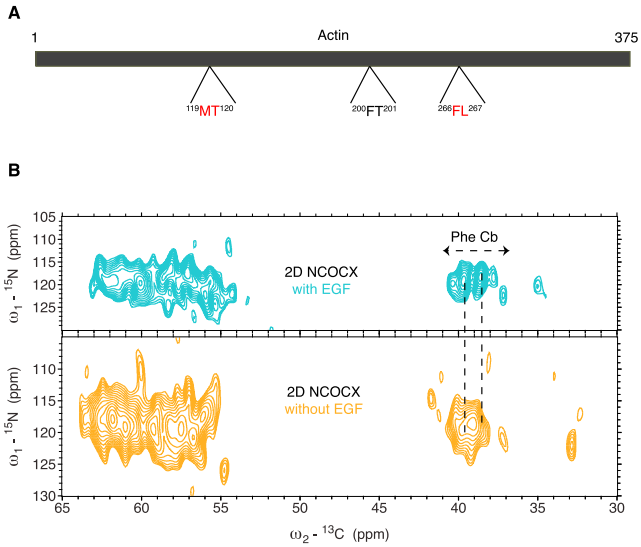

Figure S6. Sequential Correlations Predicted for Actin in the MFTL-Labeled A431 Membrane Vesicles and High-Field DNP Data, Related to Figure 5

(A) highlights the three expected correlations of Actin in the MFTL labeled A431 membrane vesicles.

(B) 2D NCOCX of MFTL labeled A431 vesicles with (cyan) and without (orange) EGF performed on a 800 MHz DNP machine (Koers et al., 2014). Dotted lines connect the Cb region of Phe in both spectra.